




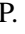

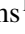


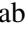




# Possible origins of anomalous H I gas around MHONGOOSE galaxy, NGC 5068<sup>★</sup>

J. Healy<sup>1</sup>, W. J. G. de Blok<sup>1,2,3</sup>, F. M. Maccagni<sup>1,4</sup>, P. Amram<sup>5</sup>, L. Chemin<sup>6</sup>, F. Combes<sup>7,8</sup>, B. W. Holwerda<sup>9</sup>,  
P. Kamphuis<sup>10</sup>, D. J. Pisano<sup>3</sup>, E. Schinnerer<sup>11</sup>, K. Spekkens<sup>12,13</sup>, L. Verdes-Montenegro<sup>14</sup>, F. Walter<sup>11</sup>,  
E. A. K. Adams<sup>1,2</sup>, B. K. Gibson<sup>15</sup>, D. Kleiner<sup>1,4</sup>, S. Veronese<sup>1,2</sup>, N. Zabel<sup>3</sup>,  
J. English<sup>16</sup>, and C. Carignan<sup>3,17,18</sup>

<sup>1</sup> Netherlands Institute for Radio Astronomy (ASTRON), Oude Hoogeveensedijk 4, 7991 PD Dwingeloo, The Netherlands  
e-mail: [juliahealyza@gmail.com](mailto:juliahealyza@gmail.com)

<sup>2</sup> Kapteyn Astronomical Institute, University of Groningen, PO Box 800, 9700 AV Groningen, The Netherlands

<sup>3</sup> Department of Astronomy, University of Cape Town, Private Bag X3, 7701 Rondebosch, South Africa

<sup>4</sup> INAF – Osservatorio Astronomico di Cagliari, Via della Scienza 5, 09047 Selargius, CA, Italy

<sup>5</sup> Aix-Marseille Univ., CNRS, CNES, LAM, 38 Rue Frédéric Joliot Curie, 13338 Marseille, France

<sup>6</sup> Instituto de Astrofísica, Facultad de Ciencias Exactas, Universidad Andrés Bello, Chile

<sup>7</sup> LERMA, Observatoire de Paris, PSL Research Université, CNRS, Sorbonne Université, 75104 Paris, France

<sup>8</sup> Collège de France, 11 Place Marcelin Berthelot, 75005 Paris, France

<sup>9</sup> University of Louisville, Department of Physics and Astronomy, 102 Natural Science Building, Louisville 40292, KY, USA

<sup>10</sup> Ruhr University Bochum, Faculty of Physics and Astronomy, Astronomical Institute (AIRUB), 44780 Bochum, Germany

<sup>11</sup> Max-Planck-Institut für Astronomie, Königstuhl 17, 69117 Heidelberg, Germany

<sup>12</sup> Department of Physics and Space Science, Royal Military College of Canada, PO Box 17000, Station Forces, Kingston, ON K7K 7B4, Canada

<sup>13</sup> Department of Physics, Engineering Physics and Astronomy, Queen's University, Kingston, ON K7L 3N6, Canada

<sup>14</sup> Instituto de Astrofísica de Andalucía (CSIC), Glorieta de la Astronomía s/n, 18008 Granada, Spain

<sup>15</sup> Astrophysics Group, Keele University, Keele, Staffordshire ST5 5BG, UK

<sup>16</sup> Department of Physics and Astronomy, University of Manitoba, Winnipeg, Manitoba R3T 2N2, Canada

<sup>17</sup> Département de physique, Université de Montréal, Complexe des sciences MIL, 1375 Avenue Thérèse-Lavoie-Roux, Montréal, QC H2V 0B3, Canada

<sup>18</sup> Laboratoire de Physique et de Chimie de l'Environnement, Observatoire d'Astrophysique de l'Université Ouaga I Pr Joseph Ki-Zerbo (ODAUO), BP 7021, Ouaga 03, Burkina Faso

Received 14 July 2023 / Accepted 12 February 2024

## ABSTRACT

The existing reservoirs of neutral atomic hydrogen gas (H I) in galaxies are insufficient to have maintained the observed levels of star formation without some kind of replenishment. This refuelling of the H I reservoirs is likely to occur at column densities an order of magnitude lower than previous observational limits ( $N_{\text{H I, limit}} \sim 10^{19} \text{ cm}^{-2}$  at a  $30''$  resolution over a linewidth of  $20 \text{ km s}^{-1}$ ). In this paper, we present recent deep H I observations of NGC 5068, a nearby isolated star-forming galaxy observed by MeerKAT as part of the MHONGOOSE survey. With these new data, we were able to detect low column density H I around NGC 5068 with a  $3\sigma$  detection limit of  $N_{\text{H I}} = 6.4 \times 10^{17} \text{ cm}^{-2}$  at a  $90''$  resolution over a  $20 \text{ km s}^{-1}$  linewidth. The high sensitivity and resolution of the MeerKAT data reveal a complex morphology of the H I in this galaxy – a regularly rotating inner disk coincident with the main star-forming disk of the galaxy, a warped outer disk of low column density gas ( $N_{\text{H I}} < 9 \times 10^{19} \text{ cm}^{-2}$ ), in addition to clumps of gas on the north-western side of the galaxy. We employed a simple two disk model that described the inner and outer disks, which enabled us to identify anomalous gas that deviates from the rotation of the main galaxy. The morphology and the kinematics of the anomalous gas suggest a possible extra-galactic origin. We explore a number of possible origin scenarios that may explain the anomalous gas, and conclude that fresh accretion is the most likely scenario.

**Key words.** galaxies: evolution – galaxies: ISM – galaxies: individual: NGC 5068 – radio lines: ISM

## 1. Introduction

How galaxies have been able to sustain the observed levels of star formation is one of the key open questions in galaxy evolution. In order for the current observed rate of star formation in the local Universe to be maintained, galaxies must refuel the gas reservoirs. How exactly this refuelling takes place is still an open question; however, it has been shown

that minor mergers alone cannot supply the required amount of gas necessary to sustain the observed levels of star formation (e.g. Di Teodoro & Fraternali 2014), meaning that some form of gas accretion must be ongoing (Larson 1972; Sancisi et al. 2008; Ho et al. 2019). There are a number of different ways this accretion of gas can occur: gas-rich mergers, the accretion of recycled gas (“fountain model” e.g. Fraternali et al. 2002; Melioli et al. 2008, 2009), or the accretion of gas from the cosmic web (van de Voort et al. 2011a; Wetzel & Nagai 2015; Cornuault et al. 2018; Ho et al. 2019; Iza et al. 2022).

<sup>★</sup> The reduced datacubes as FITS files are available at [mhongoose.astron.nl](http://mhongoose.astron.nl)

Simulations have shown that the accretion of fresh gas into galaxies generally comes in two modes (Kereš et al. 2005, 2009; Nelson et al. 2013, 2015; Huang et al. 2019). In “hot mode” accretion, the gas is shock heated as it collides with the hydrostatic hot halo near the virial radius, if the gas reaches high enough densities, it can cool and settle onto the disk. However, in “cold mode” accretion, the gas is accreted along filaments or in clumps that are not shock heated. Accretion along filaments has been shown to be more important when considering how the gas is accreted onto the galaxies (e.g. Kereš et al. 2009; van de Voort et al. 2011a; van de Voort & Schaye 2012; Hafen et al. 2020; Cadiou et al. 2022). Simulations suggest that these filaments have HI column densities of  $10^{17}$  to  $10^{18} \text{ cm}^{-2}$  (van de Voort et al. 2011a, 2019; van de Voort & Schaye 2012; Ramesh et al. 2023) which has been impossible to observe with the necessary resolution until very recently.

Unambiguously identifying accreting gas observationally is extremely difficult due to the low density of the accreting gas and the numerous different possible explanations for “accretion-like” features observed in the gas distribution of nearby galaxies. Deep observations of the HI in nearby spiral galaxies have identified the presence of extra-planar gas (EPG). This provided an opportunity to study the connection between the gas in the halo and the galaxy disk. EPG has now been identified in many spiral galaxies (see review by Sancisi et al. 2008; Marasco et al. 2019). In edge-on galaxies, such as NGC 891, the EPG is a clearly visible, extended component lagging in velocity (e.g. Swaters et al. 1997; Oosterloo et al. 2007). In studies of more face-on galaxies such as NGC 2403, the presence of the EPG is inferred by the anomalous velocities of the HI (e.g. Fraternali et al. 2001; de Blok et al. 2014; Li et al. 2023; Veronese et al. 2023). EPG has been shown to account for 10 to 20% of the total HI mass of the host galaxies (Hess et al. 2009; Gentile et al. 2013; Vargas et al. 2017; Marasco et al. 2019). There has been a concerted effort to identify the origin of EPG, particularly in relatively isolated galaxies (Heald et al. 2011; Gentile et al. 2013). While fountain models have been used to explain the presence of EPG in many galaxies (e.g. Li et al. 2023), the fountain models cannot explain all the observed EPG, suggesting other modes of accretion must also be occurring (e.g. NGC 2297, Hess et al. 2009).

In order to understand the relationship between the EPG, disk gas, and star formation, deep, high resolution HI observations in combination with multiwavelength tracers of past and ongoing star formation are needed for a representative sample of nearby ( $<20 \text{ Mpc}$ ) galaxies. High resolution (sub-kiloparsec scale) HI observations enable same-scale comparisons between the HI morphology and kinematics to tracers of star formation activity (e.g. UV and mid- or near-infrared imaging, molecular gas imaging). The high sensitivity is necessary to detect the low column density EPG HI gas. The limitations of previous generations of radio telescopes meant that surveys set out to tackle these questions had to optimise for either resolution or sensitivity.

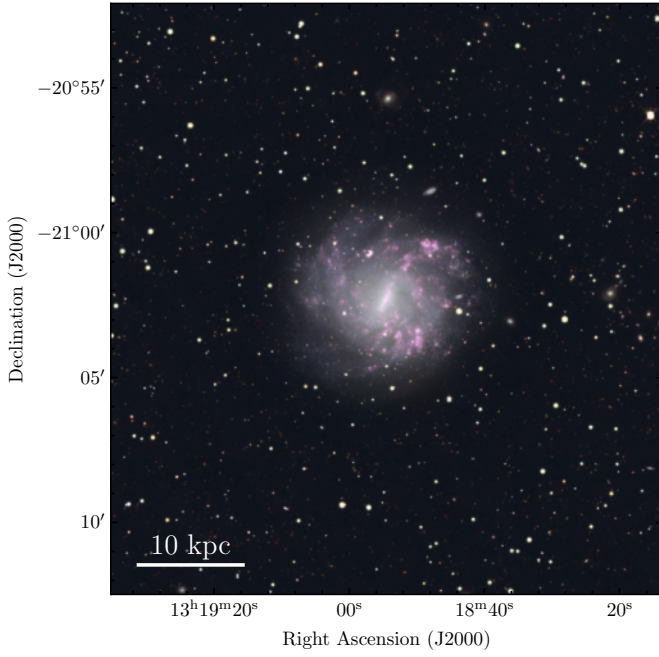
Two of these HI surveys are The HI Nearby Galaxy Survey (THINGS, Walter et al. 2008) and the Westerbork Hydrogen Accretion in Local GALaxies (HALOGAS, Heald et al. 2011) survey. THINGS is an HI survey with the Very Large Array (VLA) of 34 nearby ( $D < 15 \text{ Mpc}$ ) gas-rich spiral and dwarf galaxies. The survey made use of the VLA in B, C, and D configurations, which provided the high spatial resolution in combination with the high spectral resolution of the VLA correlator, but the HI column density sensitivity was limited to  $N_{\text{HI}} \sim 4.5 \times 10^{20} \text{ cm}^{-2}$  at  $3\sigma$  over a  $20 \text{ km s}^{-1}$  linewidth at the

highest resolution of  $6'$  (Walter et al. 2008). Some key results from THINGS include detailed analyses by Bigiel et al. (2008) and Leroy et al. (2008) of the correlation between HI and molecular hydrogen ( $\text{H}_2$ ) at sub-kiloparsec scales with star formation, showing that star formation efficiency is driven by the presence of molecular gas. Bigiel et al. (2008) also confirmed that there is a surface density at which HI saturates, and the gas is only molecular. While Leroy et al. (2008) found that where the HI component is the dominant gas phase, star formation efficiency decreases with increasing radius from the centre of the galaxy, the high resolution imaging also made it possible to detect radial motions related to the EPG component in a smaller sub-sample of THINGS galaxies (Schmidt et al. 2016). Detecting the radial motions of the gas is key to disentangling how gas is transported from the outskirts to the inner star-forming regions of galaxies with ongoing accretion.

The first systematic search for evidence of accretion of cold gas onto galaxies was the HALOGAS survey, conducted using the Westerbork Synthesis Radio Telescope, which was designed to detect the low column density HI and characterise the morphology and kinematics of the detected EPG. The 24 nearby ( $D < 20 \text{ Mpc}$ ) galaxies chosen were moderately inclined or edge-on as this makes it easier to model and study in detail the morphology and kinematics of the EPG. The deep observations ( $10 \times 12 \text{ h}$  per galaxy) provided high sensitivity HI maps ( $N_{\text{HI}} \sim 1.1 \times 10^{19} \text{ cm}^{-2}$  at  $3\sigma$  for a linewidth of  $20 \text{ km s}^{-1}$  at a resolution of  $30'$ , Heald et al. 2011). Studies of the HALOGAS galaxies have provided much of what is now known about EPG in galaxies as discussed above. Another one of the important results from HALOGAS has been the identification of clouds of anomalous gas (Heald & Team 2014; Kamphuis et al. 2022), similar to the high velocity clouds (HVC) around the Milky Way (Wakker & Van Woerden 1997). Kamphuis et al. (2022) also set important limits on the rate at which HI can be accreted via these clouds showing that it is much lower than the global accretion rate which is estimated to be  $0.2 M_{\odot} \text{ yr}^{-1}$  by Sancisi et al. (2008).

The limitations of the previous surveys have been overcome by the arrival of MeerKAT (Jonas & MeerKAT Team 2016) where it is no longer necessary to choose between sensitivity and resolution. The MeerKAT HI Observations of Nearby Galactic Objects – Observing Southern Emitters (MHONGOOSE; de Blok et al. 2016, 2020) is one of the MeerKAT Large Survey Projects, having been awarded a total of 1650 h to observe the HI in 30 nearby galaxies (55 h per galaxy). The MHONGOOSE galaxies were selected from an overlap of galaxies observed as part of both the HI Parkes All Sky Survey (HIPASS; Barnes et al. 2001; Meyer et al. 2004) and the Survey for Ionization in Neutral Gas Galaxies (SINGG; Meurer et al. 2006). This gave a first estimate of the total HI mass of the sources, and ensured the existence of ultraviolet to infrared observations of the galaxies. All 30 galaxies were also required to be within 30 Mpc, and were chosen to avoid dense environments such as the nearby Fornax and Virgo clusters. In this work, we present the new MeerKAT HI observations of one of the MHONGOOSE galaxies: NGC 5068 (HIPASS J1318–21).

NGC 5068 is a nearby,  $d = 5.2 \text{ Mpc}$  (Anand et al. 2021), close to face-on ( $i = 35.7 \pm 10.9^\circ$ , Lang et al. 2020) barred spiral galaxy (Rosolowsky et al. 2021). Table 1 provides a summary of the physical properties of the galaxy. It is an actively star-forming galaxy of intermediate stellar mass ( $M_{\star} = 2.29 \times 10^9 M_{\odot}$ , Leroy et al. 2019), located well within the scatter of the so-called star formation “main sequence”. Figure 1 shows a composite optical/FUV image of NGC 5068 which highlights the star-forming regions in the outer regions of the galaxy. Studies



**Fig. 1.** Composite optical/FUV image of NGC 5068. The DECam Legacy Survey (DECaLS; Dey et al. 2019)  $g$ ,  $r$ ,  $z$  provides the RGB colour. The far UV observed by GALEX as part of the SUNGG Survey (Wong et al. 2016) highlights the pink star formation regions.

of the HI in this galaxy, have up until now, only made use of observations by single dish telescopes (Koribalski et al. 2004; Sorgho et al. 2019; Sardone et al. 2021) which lack the resolution to identify details in the morphology of the HI disk. This work provides a first look at the high resolution details of the HI distribution of NGC 5068 while still maintaining an HI column density sensitivity equal to that of the single dish observations.

This paper is laid out as follows: in Sect. 2, we present the new MeerKAT HI observations of NGC 5068 and the process by which we calibrated and imaged the data. In Sect. 3 we discuss the global HI properties of the galaxy, and compare to previously published observations. A detailed discussion on the kinematics of the HI follows in Sect. 4. Finally, in Sect. 5, we explore different possible origins of the anomalous low column density HI gas detected in NGC 5068.

## 2. MeerKAT observations

NGC 5068 was observed as part of MHONGOOSE in ten 5.5 h tracks (inclusive of time spent on the calibrators) for a total on-source time of 50 h. In each track, the primary calibrator, J0408–6545 (rising tracks) or J1939–6342 (setting tracks), was observed for 10 min. The secondary calibrator, J1311–2216, was observed every 50 min for 2 min. The observations were carried out at night between April 2021 and March 2022 using an average of 62 of the 64 antenna which provide baselines of 29 to 7800 m. Each MeerKAT dish has a diameter of 13.5 m which corresponds to a full width at half max (FWHM) of the primary beam of 55 arcmin at  $\nu = 1420.405$  MHz; for more details see de Blok et al. (2024).

Each track was observed using the narrow-band (107 MHz) mode of MeerKAT. With this mode, the observations have a native channel width of 3.3 kHz or  $0.7 \text{ km s}^{-1}$  at 1420 MHz. We bin the channels by a factor of two, to a channel width of 6.6 kHz or  $1.4 \text{ km s}^{-1}$ , before starting the calibration process. Due to

**Table 1.** General properties of NGC 5068.

$\alpha, \delta$ (J2000)	13 <sup>h</sup> 18 <sup>m</sup> 54.5 <sup>s</sup> –21°02′17″
$v_{\text{sys}}$ (km s <sup>-1</sup> )	$667.8 \pm 1.3$ <sup>(a)</sup>
PA (°)	$342.4 \pm 3.2$ <sup>(b)</sup>
$i$ (°)	$35.7 \pm 10.9$ <sup>(b)</sup>
$D_{25}$ (′)	7.03 <sup>(c)</sup>
$d$ (Mpc)	$5.20 \pm 0.22$ <sup>(d)</sup>
$M_{\star}$ ( $M_{\odot}$ )	$2.29 \times 10^9$ <sup>(e)</sup>
SFR ( $M_{\odot} \text{ yr}^{-1}$ )	$0.275 \pm 0.127$ <sup>(e)</sup>

**Notes.** <sup>(a)</sup>Calculated from the global profile in this work. <sup>(b)</sup>Based on optical properties from Lang et al. (2020). <sup>(c)</sup>B-band diameter at 25 mag arcsec<sup>-2</sup> isophote from Lauberts & Valentijn (1989). <sup>(d)</sup>TRGB from Anand et al. (2021). <sup>(e)</sup>Leroy et al. (2019).

the shape of the MeerKAT spectral response (van der Byl et al. 2022) individual  $0.7 \text{ km s}^{-1}$  channels are independent, implying that our binned  $1.4 \text{ km s}^{-1}$  channels are as well.

All ten tracks were calibrated using the same procedure with version 1.0.5 of the Containerized Automated Radio Astronomy Calibration (CARAcal) pipeline (Józsa et al. 2020). CARAcal provides a single environment in which to carry out the usual calibration and reduction steps: flagging of data, cross-calibration, splitting of the target, self-calibration, and later the continuum subtraction and spectral line imaging and deconvolution. At each step, the pipeline produces diagnostic plots which help to identify any issues that may arise. These are consolidated outside of CARAcal into a calibration report for each track that is automatically uploaded and stored on a private GitHub team repository where each report is used to quality check the observation.

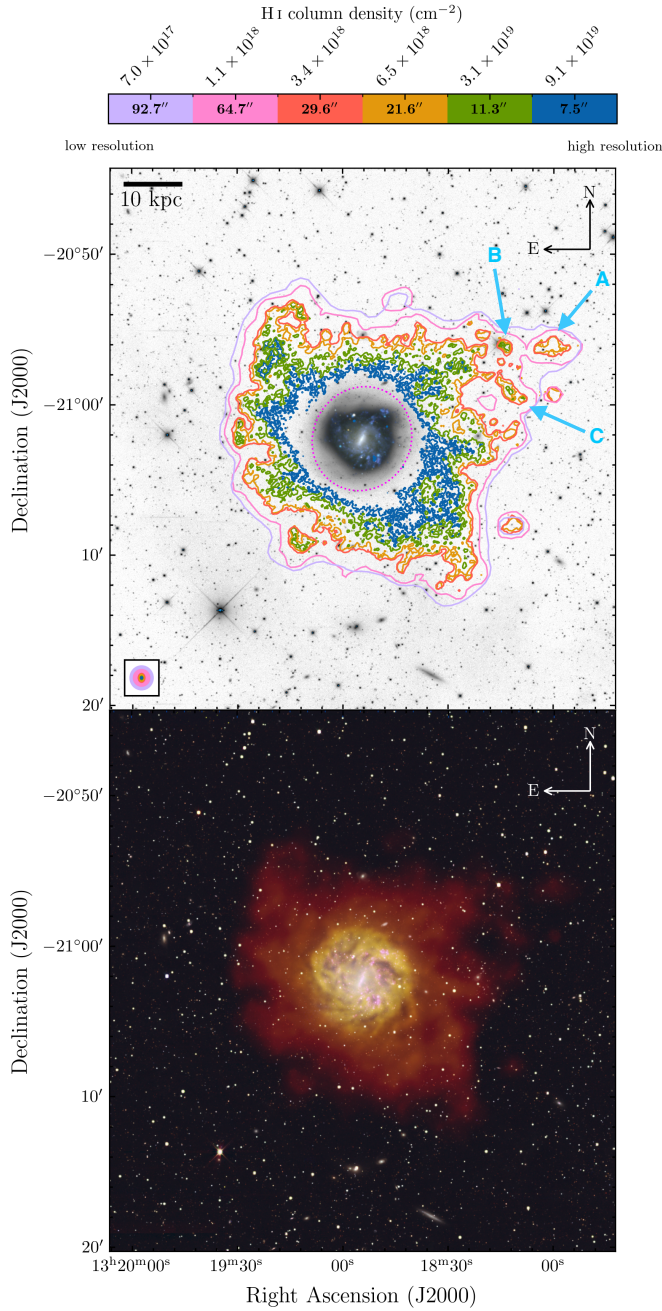
### 2.1. Self calibration and continuum subtraction

We used self-calibration of the continuum to further improve the quality of the calibration. For this we used a continuum image created from the frequency range 1390–1422 MHz, taking care to flag the frequency range covered by the HI emission from both the Galaxy and the target, NGC 5068. Four rounds of self-calibration were used, where in each round a progressively lower signal-to-noise (S/N) threshold is employed to create a mask using the Source Finding Application (SoFiA, Serra et al. 2015), which thus increases the number of sources to be included in the progressively better sky model. The continuum emission of NGC 5068 is bright and extended, and we note the importance of including all of the diffuse continuum emission of NGC 5068 in the sky model. Not doing so leads to the appearance of “ghosts” in the data, mimicking faint HI structures (Grobler et al. 2014; Wijnholds et al. 2016). The model is also used in the first continuum subtraction step for the HI spectral line cube. Any residual continuum emission is subtracted using a 1st order polynomial fit to the line-free channels.

### 2.2. HI imaging

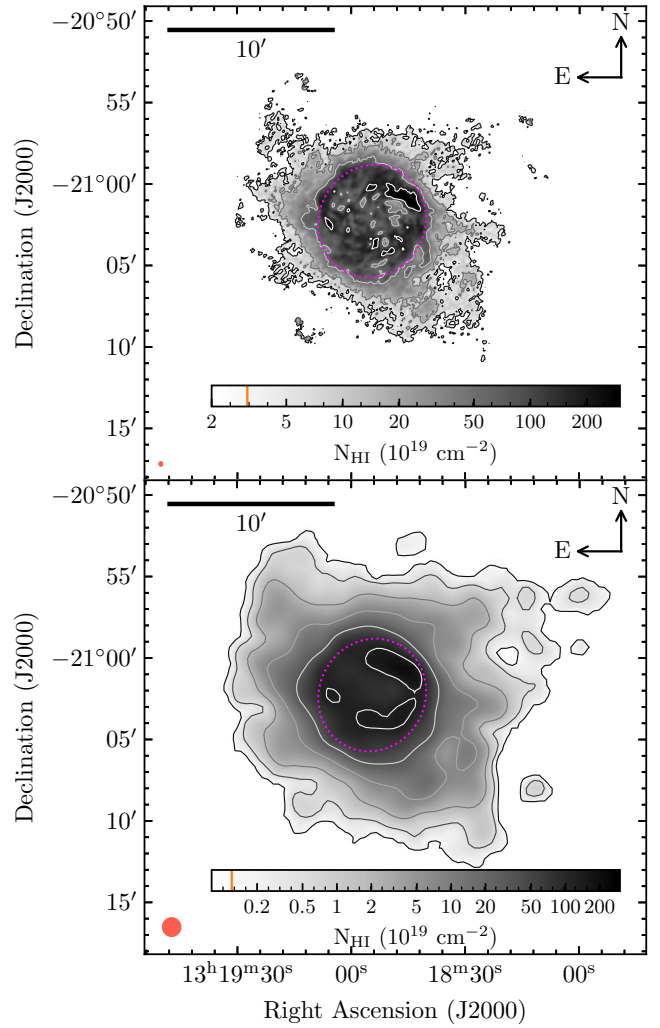
The HI cubes were imaged using WSClean (Offringa et al. 2014; Offringa & Smirnov 2017) as part of CARAcal. We employed a 3-step iterative strategy to cleaning the HI data: first, a low-resolution cube was created and cleaned using a  $5\sigma_{\text{rms}}$  clip WSClean auto-mask. From this low-resolution cube, a mask of





**Fig. 2.** Overview of the optical and H I emission of NGC 5068. Top: greyscale MeerLICHT  $q$ -band image and colour with contours from the six different resolution H I cubes. The contours correspond to colours in the colourbar which indicate the resolution and the H I column density at the  $S/N = 3$  contour in the intensity maps. Three clouds associated with the galaxy are labelled A, B, C. Dotted magenta ellipse indicates the optical extent of the galaxy. The beam for resolution (contour) is shown in the corresponding colour in the box in the bottom left corner. Bottom: H I emission combined with Fig. 1. The red, orange, and yellow show moment 0 maps of the H I emission from the 64.7'' (r05\_t60), 29.6'' (r10\_t00), and 7.5'' (r00\_t00) resolution H I cubes respectively. Production of this image followed English (2017), including the technique of masking in order to combine the data sets and reveal the optical data's H II regions (light pink).

the source was created using SoFia-2 (Westmeier et al. 2021); second, using the newly created low resolution mask for the cleaning, we created a new cube at the desired resolution from



**Fig. 3.** Integrated intensity (moment 0) maps of NGC 5068. In the top panel is the map from one of the high resolution cubes (r05\_t0) at 11'', and in the bottom panel is a map from one of the low resolution cubes (r05\_t60) at 64''. The dashed magenta ellipse is centred on the optical centre of the galaxy and represents the extent of the optical disk. The contours increase as  $\sigma_{S/N=3} \times 2^n$ ,  $n = 0, 2, 4, 6, \dots$ . The lowest contour plotted is the  $S/N = 3$  contour,  $N_{\text{HI}} = 3.1 \times 10^{19} \text{ cm}^{-2}$  for the top panel and  $N_{\text{HI}} = 1.1 \times 10^{18} \text{ cm}^{-2}$  for the bottom panel, these  $S/N = 3$  ( $n = 0$ ) values are indicated on the respective colour bars by the orange line. The red ellipse in the bottom left corner of each panel represents the beam.

which an updated clean-mask was created using SoFia-2; in the third step, the final H I cubes that are presented in this work were created and cleaned using the updated mask from the previous step. In each step, we cleaned the data to  $0.5\sigma_{\text{rms}}$ . This procedure is described in more detail in the MHONGOOSE paper presenting the full survey sample (de Blok et al. 2024).

We make full use of MeerKAT's resolution and sensitivity capabilities by creating a set of six H I cubes with a  $1.5^\circ$  field of view (FoV) that range in resolution ( $7''$  to  $90''$ ) which correspond to  $0.34 \text{ kpc}$  to  $4 \text{ kpc}$ . This is done using different combinations of robust weighting ( $r$ ) and Gaussian tapering ( $t$ ), which varies the noise and resolution, and thus the H I column density sensitivity ( $N_{\text{HI}} \sim 6.8 \times 10^{19} \text{ cm}^{-2}$  to  $6.4 \times 10^{17} \text{ cm}^{-2}$  at  $3\sigma$  over  $20 \text{ km s}^{-1}$  – see Table 2). The combinations are listed in the left-most column of Table 2. Using this broad range in sensitivity and resolution, we can characterise the morphology of the H I.



**Table 2.** Properties of the H I cubes.

Cube	Resolution (arcsec $\times$ arcsec)	Pixel size (arcsec)	$\sigma_{\text{rms}}^{(a)}$ (mJy beam $^{-1}$ )	$N_{\text{H I}} (3\sigma \text{ over } 20 \text{ km s}^{-1})^{(c)}$ (cm $^{-2}$ )	$N_{\text{H I}} (S/N = 3)^{(d)}$ (cm $^{-2}$ )
$r = 0.0, t = 0''^{(b)}$	$8.1 \times 6.9$	2	0.215	$6.8 \times 10^{19}$	$9.1 \times 10^{19}$
$r = 0.5, t = 0''$	$13.4 \times 9.4$	3	0.169	$2.3 \times 10^{19}$	$3.1 \times 10^{19}$
$r = 1.0, t = 0''$	$26.0 \times 17.9$	5	0.148	$5.6 \times 10^{18}$	$6.5 \times 10^{18}$
$r = 1.5, t = 0''$	$34.3 \times 25.6$	7	0.153	$3.1 \times 10^{18}$	$3.4 \times 10^{18}$
$r = 0.5, t = 60''$	$65.3 \times 63.8$	20	0.241	$1.0 \times 10^{18}$	$1.1 \times 10^{18}$
$r = 1.0, t = 90''$	$93.8 \times 91.7$	30	0.313	$6.4 \times 10^{17}$	$7.0 \times 10^{17}$

**Notes.** <sup>(a)</sup>This is measured per  $1.4 \text{ km s}^{-1}$  channel. <sup>(b)</sup> $r$  is the robust weighting, and  $t$  the Gaussian taper. <sup>(c)</sup>Based on  $3\sigma$  detection in 14 channels. <sup>(d)</sup>Mean column density at the  $S/N = 3$  contour in the moment 0 map, see Sect. 3.1 for details.

Also listed for completeness in Table 2 is the resolution (second column), the  $\sigma_{\text{rms}}$  based on  $1.4 \text{ km s}^{-1}$  wide channels (fourth column),  $3\sigma$  over  $20 \text{ km s}^{-1}$  column density sensitivity (fifth column), and the column density at  $S/N = 3$  in the total intensity maps (sixth column) for each cube.

### 3. Global H I properties

#### 3.1. Morphology of the H I disk

The six H I cubes enable us to explore both the details of the dense H I in the galaxy disk, as well as the low column density EPG. For each cube we create a suite of moment maps by using SoFiA-2 to identify all detectable H I emission in the velocity range ( $200 < v_{\text{rad}} (\text{km s}^{-1}) < 1143$ ) covered by the data cube. We used the smooth and clip algorithm to identify all signal above a threshold of  $3.5\sigma$  using using all combinations of the following spatial and spectral smoothing kernels: spatially, these are the original resolution and a spatial smoothing kernel equal to the synthesised beam; spectrally, we used the original resolution and kernels of 9 channels ( $\sim 12 \text{ km s}^{-1}$ ), and 25 channels ( $\sim 35 \text{ km s}^{-1}$ ). The source finding yields the H I emission associated with only the target galaxy, NGC 5068, within a field of view of  $1.5^\circ$  which corresponds to a radius of 125 kpc. The primary beam<sup>1</sup> corrected moment maps are created from the masked data cubes, however we further limit the first moment (intensity-weighted mean velocity field) and second moment (sometimes referred to as the velocity dispersion map) maps to only include the pixels where the integrated H I column density ( $N_{\text{H I}}$ ) is greater than the  $S/N = 3$  threshold. This threshold is determined for each resolution map by using the  $S/N$  map output by SoFiA-2 where  $S/N = \sum S dv / (\sigma_{\text{rms}} dv \sqrt{N_{\text{chan}}})$ ,  $S dv$  is the moment zero,  $\sigma_{\text{rms}}$  is the noise per channel of the H I cube,  $dv$  is the channel width, and  $N_{\text{chan}}$  is the number of channels of the H I cube that contributes to each pixel of the zeroth moment map. This is only valid under the assumption that the channels are independent which in this case is true as the observed channels were binned in pairs and no Hanning smoothing was used. Following Meyer et al. (2017, Eq. (75)), we calculate the  $N_{\text{H I}, S/N=3}$  threshold by calculating the median column density of the pixels which are in the range  $2.75 < S/N < 3.25$  in the  $S/N$  map. Despite the differences in how the values are calculated, the  $N_{\text{H I}, 3\sigma}$  and  $N_{\text{H I}, S/N=3}$  values presented in Table 3 Cols. 5 and 6 respectively, are similar although the  $N_{\text{H I}, S/N=3}$  values tend to be slightly higher. This is due to a combination of the smooth

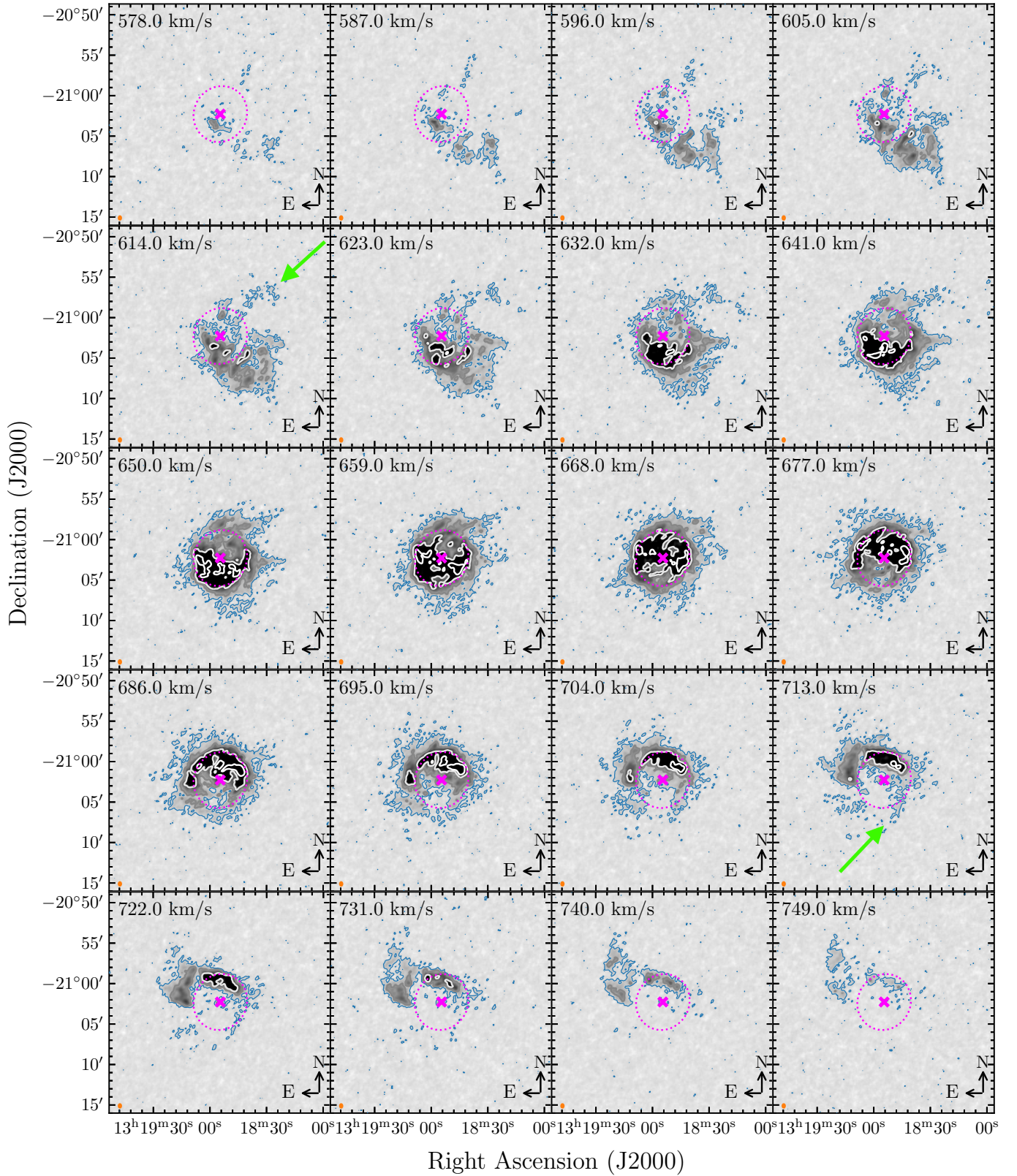
and clip algorithm used to identify emission associated with a detection, and the linking lengths used in SoFiA-2 to add pixels containing emission to the detection mask which results in a mask that is wider than what would be created using a simple  $3\sigma$  clip. It is worth noting that the column density limits presented in Table 3 are significantly lower than the previous generation of H I column density limits, and reflect the excellent quality of these deep MeerKAT data.

The top panel of Fig. 2 shows the  $N_{\text{H I}}(S/N = 3)$  contours of the H I distribution seen in the different resolutions plotted on the MeerLICHT (Bloemen et al. 2016)  $q$ -band<sup>2</sup> image which has a  $5\sigma$  surface brightness limit of  $24.61 \text{ mag arcsec}^{-2}$ . MeerLICHT is a 0.6 m optical telescope, located in Sutherland, South Africa, with a  $1.6^\circ \times 1.6^\circ$  FoV ( $\sim 1.7 \times \text{FWHM}$  of the MeerKAT primary beam at  $z = 0$ ). The bottom panel of Fig. 2 combines H I moment maps with Fig. 1 and shows spatial relationships between the star-forming regions and atomic gas structures in the form of H I densities or cavities. The upper panel shows the extent of the gas at different column density levels, with the low column density gas extending out to more than 2.5 times the optical radius, defined by the  $B$ -band  $25 \text{ mag arcsec}^{-2}$  isophote (Lauberts & Valentijn 1989), of the galaxy which is approximately 10 kpc. Figure 2 also shows finger-like tendrils of H I extending out from the optical disk at column densities of  $N_{\text{H I}} \sim 3.1$  to  $9.7 \times 10^{19} \text{ cm}^{-2}$  (green contour). Also of interest are the low-column density clumps on the north-western side of the galaxy which were identified by eye. These clumps appear as distinct clouds below H I column densities of  $N_{\text{H I}} \sim 3 \times 10^{19} \text{ cm}^{-2}$  but become connected to the galaxy H I disk in the  $60''$  (pink) and  $90''$  (purple) resolution cubes which is likely a resolution effect. The more prominent clumps have been labelled A, B, C in the top panel of Fig. 2. While Fig. 2 provides an overall picture of the total H I intensity distribution, to be able to study the different features, it is necessary to examine the individual moment 0 maps at the various resolutions.

Figure 3 shows the moment 0 (H I intensity) maps at two different resolutions:  $11''$  ( $0.5 \text{ kpc}$ ) and  $64''$  ( $3 \text{ kpc}$ ). In the top panel the high resolution (r05\_t0 which corresponds to the robust ( $r$ ) = 0.5 and taper ( $t$ ) =  $0''$  cube) map highlights the clumpy nature of the H I, in particular the finger-like tendrils and the clouds on the outskirts of the galaxy. The optical disk is represented by the dotted magenta ellipse measured as the diameter of the  $25 \text{ mag arcsec}^{-2}$  isophote ( $D_{25}$ ) in the  $B$ -band by Lauberts & Valentijn (1989). In the bottom panel of Fig. 3, the lower resolution (r05\_t60) map shows the extent of the

<sup>1</sup> The MeerKAT primary beam FWHM is  $55'$  at  $z = 0$ , this entirely contains the H I of NGC 5068 which spans roughly  $30'$ .

<sup>2</sup> The MeerLICHT  $q$ -band is a wide-band that covers the  $g$  and  $r$  bands.



**Fig. 4.** Channel maps taken from the `r10_t0` cube that has been smoothed with a 5 channel Hanning window and regridded to  $3 \text{ km s}^{-1}$  channels. Every third  $3 \text{ km s}^{-1}$  channel for a  $170 \text{ km s}^{-1}$  range centred on the systemic velocity is shown. The blue contour indicates  $3\sigma_{\text{rms}}$ , the greyscale contours are  $3\sigma_{\text{rms}} \times 2^n$ ,  $n = 2, 4, 6, \dots$ . The magenta cross indicates the optical centre of the galaxy, and dotted magenta ellipse indicates the extent of the optical disk ( $D_{25}$ ) of the galaxy. The green arrows point to “fingers” in the H I. The orange ellipse in the lower left corner of each panel represents the  $21.6''$  beam.

**Table 3.** Global H I properties of NGC 5068 measured from the global profile.

Parameter	Value
$S_{\text{int}}$	$167.82 \pm 0.15 \text{ Jy km s}^{-1}$
$M_{\text{HI}} \text{ (total)}$	$1.07 \pm 0.09 \times 10^9 M_{\odot}$
$w_{50}$	$67.1 \pm 0.6 \text{ km s}^{-1}$
$w_{20}$	$109.1 \pm 2.0 \text{ km s}^{-1}$
$v_{\text{sys}}$	$667.8 \pm 1.3 \text{ km s}^{-1}$

low column density gas which connects the clouds visible in the higher resolution map to the H I in the galaxy.

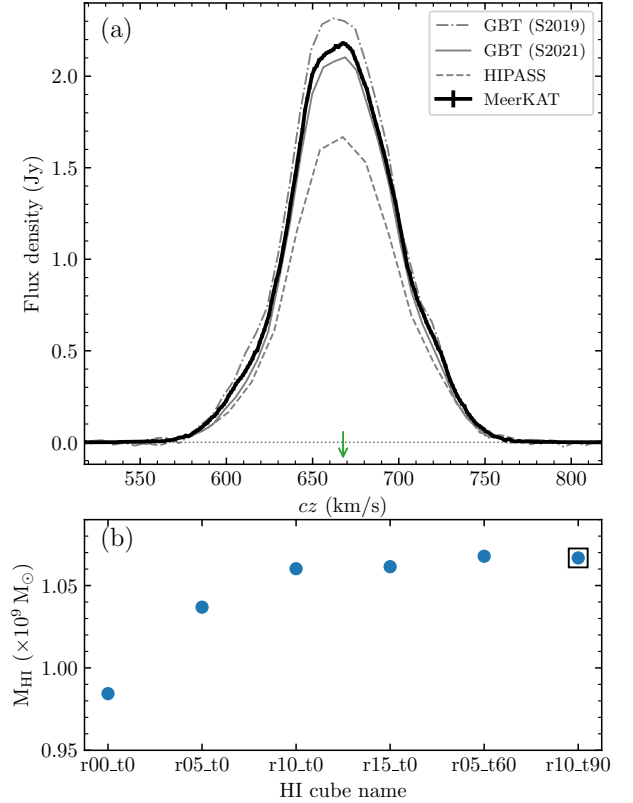
The individual channel maps provide a clearer picture of the fingers and clouds. Figure 4 shows a selection of channels taken from the  $r = 1$ , no taper (r10\_t0) cube, which has a resolution of  $21.6''$ , that has been Hanning-smoothed with a 5 channel kernel and regridded to a channel width of  $3 \text{ km s}^{-1}$  to increase the signal to noise of the lowest column density features. This smoothed version of the r10\_t0 cube provides a good balance between resolution and column density sensitivity. We note two distinct features that are evident in the channel maps: the first being two “fingers”, one which points out towards the north–west (NW) and the other pointing towards the south–east (SE) – both indicated by the green arrows in the figure. The second feature is that there appears to be two disks: one inner disk that has a major axis running approximately NW–SE and is coincidental with the optical disk, and the second outer disk which appears to be more elliptical and has a major axis running approximately NE–SW.

The global profile, extracted from the  $r = 1.0$ ,  $t = 90''$  (r10\_t90) cube using the associated SoFiA-2 mask, is shown in panel a of Fig. 5. For each resolution cube, we determine the mass encapsulated by the mask, the values are shown in panel b. It is clear that the H I mass does not change significantly between the largest four resolutions which suggests that all the H I mass for the system has been identified. The robust weighting used to create the lower resolution H I cubes emphasises the shorter baselines making these measurements more suitable for computing the total H I mass.

From the global profile in Fig. 5, we calculated the total integrated flux, the line width at 50% ( $w_{50}$ ) and 20% ( $w_{20}$ ) of the peak flux are measured directly from the profile, and we determine the systemic velocity to be the velocity at the mid point of the  $w_{20}$ . These values are listed in Table 3. While the largest contribution to the flux uncertainty are from the systematics arising as part of the calibration process, the uncertainties on the global profile are calculated base on the noise properties of the corresponding H I cube.

### 3.2. Comparison with previous observations

Here we compare the total H I flux of NGC 5068 with those obtained from single-dish measurements from the H I Parkes All Sky Survey (HIPASS, Meyer et al. 2004; Koribalski et al. 2004) and targeted observations using the Green Bank Telescope (GBT, Sorgho et al. 2019; Sardone et al. 2021). Sorgho et al. (2019) and Sardone et al. (2021) analysed a sub-sample of the MHONGOOSE galaxies using GBT. Although they use the same GBT spectra, they process the data differently which resulted in slightly different global profiles and measurements of the integrated flux for NGC 5068. The total integrated flux mea-



**Fig. 5.** (a) Global H I profile of NGC 5068 from MeerKAT (black), HIPASS (dashed grey line; Koribalski et al. 2004), GBT (solid grey and dot-dash grey line; Sorgho et al. 2019; Sardone et al. 2021). The green arrow indicates the systemic velocity of the galaxy. (b) The H I mass of NGC 5068 measured within the SoFiA-2 mask for each different resolution cube. The open black square indicates which cube was used to create the global profile shown in the top panel.

surements from each survey are listed in Table 4, and the global profiles are also plotted in Fig. 5a.

As is evident from Table 4, there are differences in measured fluxes between the different single-dish measurements. Despite the differences in the integrated fluxes, the H I global profile line widths ( $w_{20}$  and  $w_{50}$ ) measured for NGC 5068 by Sorgho et al. (2019) and Sardone et al. (2021) from the GBT observations, and by Koribalski et al. (2004) from HIPASS are consistent with what we measure from the MeerKAT spectra.

While the shape and amplitude of the Sardone et al. (2021) global profile is consistent with the MeerKAT spectrum, the quoted integrated flux is inconsistent. The higher flux density measurement quoted in Sardone et al. (2021) is due to how the value was calculated: they determined the total flux density of the galaxy by measuring the flux in annuli with increasing radius from the galaxy centre, and then summing the flux in all the annuli. This method of determining the total flux of the galaxy is not the same as the integrated flux based on the global profile. We recalculated the integrated flux from the Sardone et al. (2021) global profile to be  $S_{\text{HI}} = 157.7 \text{ Jy km s}^{-1}$  which is consistent within 10% of the MeerKAT value.

Given that we do not expect the HIPASS observations of NGC 5068 to be missing any flux, it is therefore curious that there is such a large discrepancy between the total integrated flux measured from the MeerKAT spectrum and that which is reported by Koribalski et al. (2004). However, the HIPASS data are known to underestimate the H I emission of large galaxies as a result



**Table 4.** Total integrated flux and linewidth measurements for NGC 5068 from different HI surveys.

Survey	Integrated flux (Jy km s <sup>-1</sup> )	w <sub>20</sub> (km s <sup>-1</sup> )	w <sub>50</sub> (km s <sup>-1</sup> )
HIPASS (Koribalski et al. 2004)	128.6 ± 12.7	111.0	70.0
GBT (Sorgho et al. 2019)	177.0 ± 0.7	–	69.3
GBT (Sardone et al. 2021)	191.5 <sup>(a)</sup>	108.0	67.9
MeerKAT (this work)	167.82 ± 0.15	109.1 ± 2.0	67.1 ± 0.6

**Notes.** <sup>(a)</sup> $S_{\text{HI}} = 157.7 \text{ Jy km s}^{-1}$  measured from the global profile assuming a gain of  $1.86 \text{ K Jy}^{-1}$  from Sardone et al. (2021).

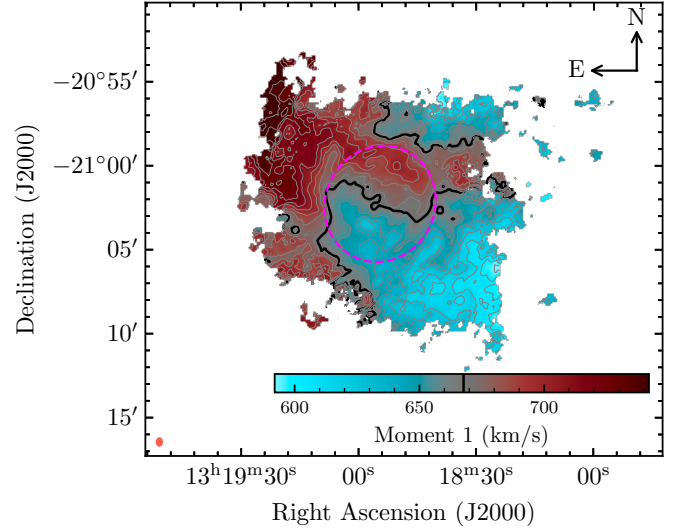
of the bandpass correction method (Barnes et al. 2001) which likely subtracted some of the HI (see de Blok et al. 2024 for a detailed comparison with all 30 MHONGOOSE galaxies).

#### 4. Kinematics of the HI

In Fig. 6, we present the intensity weighted mean velocity field (moment 1) from the **r10\_t0** cube at  $21.6''$ . For this analysis, we use the **r10\_t0** cube as it provides a good combination of resolution and HI column density sensitivity. The systemic velocity ( $v_{\text{sys}}$ , listed in Table 3) is measured as the central velocity of the global profile – this is a reasonable assumption given the symmetry of the global profile. The  $v_{\text{sys}}$  is indicated by the green arrow in Fig. 5, and by the thick black contour in Fig. 6. The HI kinematics presented in Fig. 6 are rather complex, but there appears to be at least three main components to the velocity field: (1) a regularly rotating inner disk with a mass measured within the  $\Sigma_{\text{HI}} = 1 M_{\odot} \text{ pc}^{-2}$  contour of  $M_{\text{disk}} = 9.7 \times 10^8 M_{\odot}$ ; (2) a separate, inclined warped “disk” which extends to larger radii than the optical disk, that has an HI mass of  $M_{\text{outer}} = 8.9 \times 10^7 M_{\odot}$ , calculated as all the HI outside the inner disk (including the third component); (3) the northern and north-western quadrant which is home to the clumpy clouds identified in Fig. 2 which make up on average  $8.9 \times 10^4 M_{\odot}$  each, with the most massive being C at  $1.6 \times 10^5 M_{\odot}$ .

The first component is the regularly rotating main inner disk that is coincident with the optical body represented by the magenta ellipse in Fig. 6. We find that the  $\Sigma_{\text{HI}} = 1 M_{\odot} \text{ pc}^{-2}$  contour (which is roughly equivalent to  $1.2 \times 10^{20} \text{ cm}^{-2}$ , the second lowest contour in the top panel of Fig. 3) neatly encircles this region of the velocity field. This contour ( $\Sigma_{\text{HI}} = 1 M_{\odot} \text{ pc}^{-2}$ ) is usually used to determine the HI diameter of galaxies (e.g. Wang et al. 2016), a parameter that has a very tight correlation with the HI mass. The contour is also roughly 20 to 50% larger than the optical disk (see top panel of Fig. 3), which is consistent with other measurements of late type galaxies (Bosma 2016). Compared to the total HI mass of the system (see Table 5), the inner disk ( $M_{\text{disk}} = 9.7 \times 10^8 M_{\odot}$ ) clearly makes up the majority ( $\sim 90\%$ ) of the HI mass of the galaxy.

A position velocity (PV) diagram extracted along the optical major axis (see Table 1) is presented in Fig. 7. The PV slice is extracted using the width of the beam ( $21.6''$ ) from the **r10\_t0** cube that has been Hanning smoothed and regridded to  $3 \text{ km s}^{-1}$ . The PV slice shows that while in the region corresponding to the optical disk (denoted by the vertical magenta lines) there is regular rotation as seen in the velocity field (Fig. 6). The light green circles overlaid on the PV slice in Fig. 7 indicate the moment 1 velocity in each line of sight. Anomalous gas is clearly visible in the PV slice, indicated by the regions of gas deviating from the regular rotation and extending to higher and



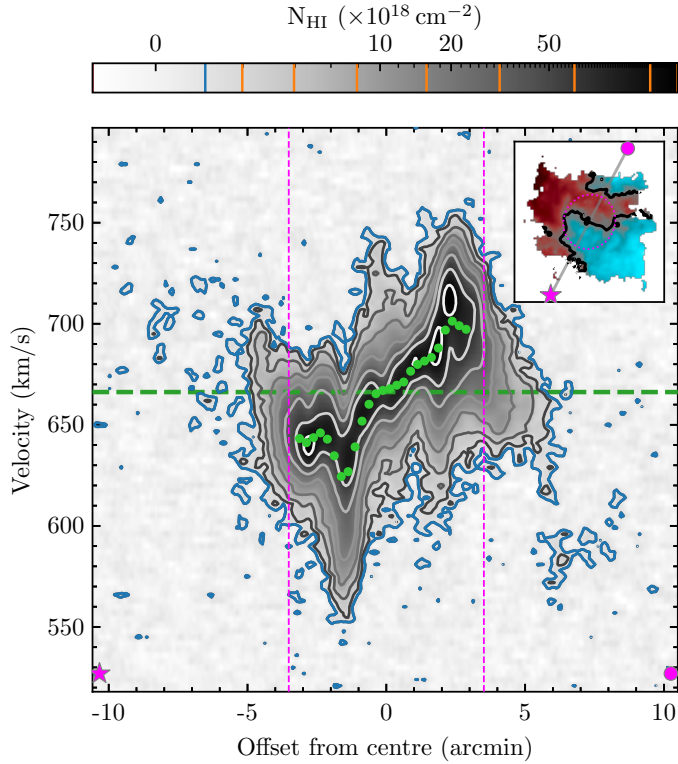
**Fig. 6.** Velocity field (moment 1) for NGC 5068. Pixels with an HI column density below  $N_{\text{HI}} = 5.9 \times 10^{18} \text{ cm}^{-2}$  ( $S/N = 3$ ) are masked. The colourbar in the bottom of the image indicates the velocity of the gas, the grey contours are spaced  $10 \text{ km s}^{-1}$  apart with the black contour indicating the systemic velocity,  $v_{\text{sys}} = 667 \text{ km s}^{-1}$ . The dotted magenta ellipse is centred on the optical centre of the galaxy and represents the optical size of the galaxy.

**Table 5.** HI mass measurements of the different components of the HI disk of NGC 5068.

Component	HI mass ( $M_{\odot}$ )
$M_{\text{HI, total}}$	$1.07 \times 10^9$
$M_{\text{disk}}$	$9.7 \times 10^8$
$M_{\text{outer}}$	$8.9 \times 10^7$
Average $M_{\text{clumps}}$	$8.9 \times 10^4$
$M_{\text{HI}}$ (residual clumpy gas)	$2.6 \times 10^7$

lower velocities. The sudden dip in velocity on the approaching side of the galaxy at roughly  $-1.4'$  offset from the centre has similar characteristics to the HI holes identified in NGC 6946 (Kamphuis & Sancisi 1993; Boomsma et al. 2008), and M 31 and M 33 (Deul & den Hartog 1990). While the kinematics of the feature are similar to the NGC 6946 holes, there is no obvious hole in the morphology of the HI. Thus it is more likely that the feature in the PV diagram is indicative of some kind of expanding feature or shell or a hole that has not blown out yet which is why there is no corresponding feature in the intensity map. Features such as holes or shells in the HI distribution are thought to be caused by energetic processes such as supernovae or stellar winds. Since this dip in the PV slice coincides with emission in the continuum and far-UV, both tracers of ongoing and recent star formation, it is likely the aforementioned processes are responsible for the feature. Another noteworthy feature of the PV slice is that there is clearly low column density extraplanar gas distributed throughout the disk.

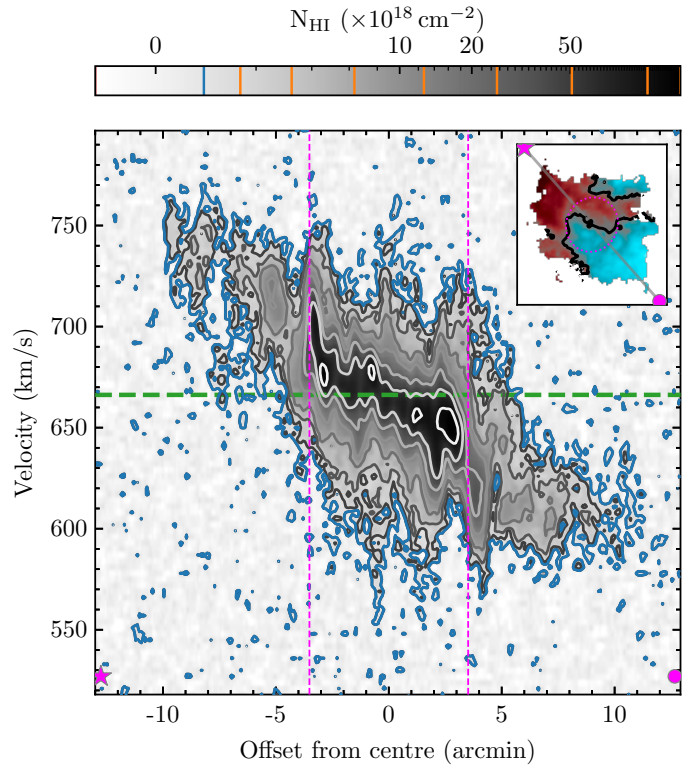
The second component is comprised of the low column density gas ( $N_{\text{HI}} < 10^{19} \text{ cm}^{-2}$ ) at radii larger than the inner disk. The gas in this component appears to have disk-like kinematics with a position angle of  $\sim 224^\circ$ . In Fig. 8 we present a PV diagram through the centre of NGC 5068 at this angle which shows clearly the rotation of this component at larger radii than the inner disk (represented by the vertical magenta lines in the



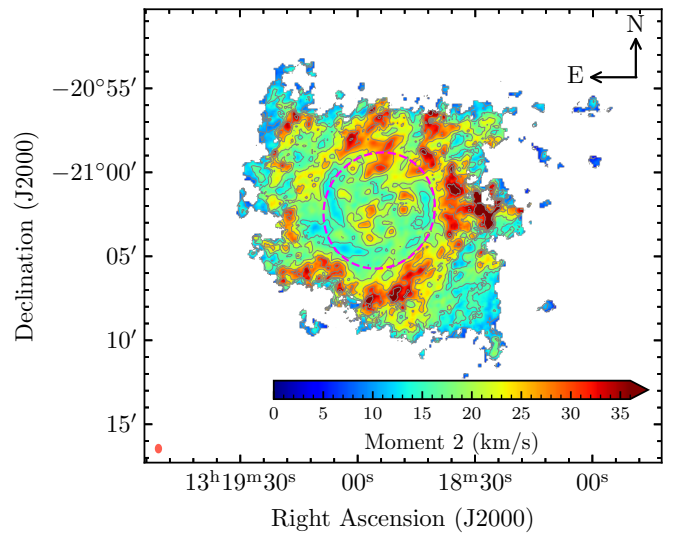
**Fig. 7.** Position-velocity diagram extracted with a width of  $21.6''$  which corresponds to the size of the beam. The slice is extracted along optical major axis. The inset on the top right of the figure shows the velocity field from Fig. 6, the grey line running from the magenta star to the filled circle represent the path along which the PV slice was extracted, the magenta star and circle are located in the lower left and upper right corners indicating the direction of the slice, these symbols are repeated lower left and right corners of the main figure. The horizontal dashed green line indicates the systemic velocity, while the light green filled circles show the moment 1 velocity at each position along the major axis. The dashed vertical magenta lines correspond to the edge of the optical disk represented by the dotted magenta ellipse in the inset. The blue and orange contours in the colour bar correspond to the blue and greyscale contours on the PV slice.

figure). The elliptical geometry of this component suggests that it is more inclined than the inner disk – approximately  $i \sim 53^\circ$ . A closer look at the kinematics in Fig. 6 show that the outer regions are twisted in an S-shape which suggests a warp. Deep  $r$ - ( $\mu_{3\sigma} = 26.5 \text{ mag arcsec}^{-2}$ ) and  $g$ -band ( $\mu_{3\sigma} = 27.2 \text{ mag arcsec}^{-2}$ ) imaging from the DECam Legacy Survey (DECaLS, Dey et al. 2019) Data Release 10 (DR10) shows that there is no stellar counterpart associated with this gas.

The differences in the position angle and inclination between this component and the inner disk suggest that this outer disk is not as a result of gas being swept out of the inner disk, but rather it has a separate origin. Given the kinematics and the geometry of the outer disk relative to the inner disk, we describe it as a warped inclined outer disk which could possibly be a warped polar disk. Characteristically polar disks are highly inclined relative to the inner disk and the position angles can also be very different to that of the inner disk – see the prototypical examples of NGC 4650A (Arnaboldi et al. 1997) and NGC 660 (Gottesman & Mahon 1990; van Driel et al. 1995). Without proper modelling (see Deg et al., in prep. for detailed modelling of polar disk galaxy candidates), the polar



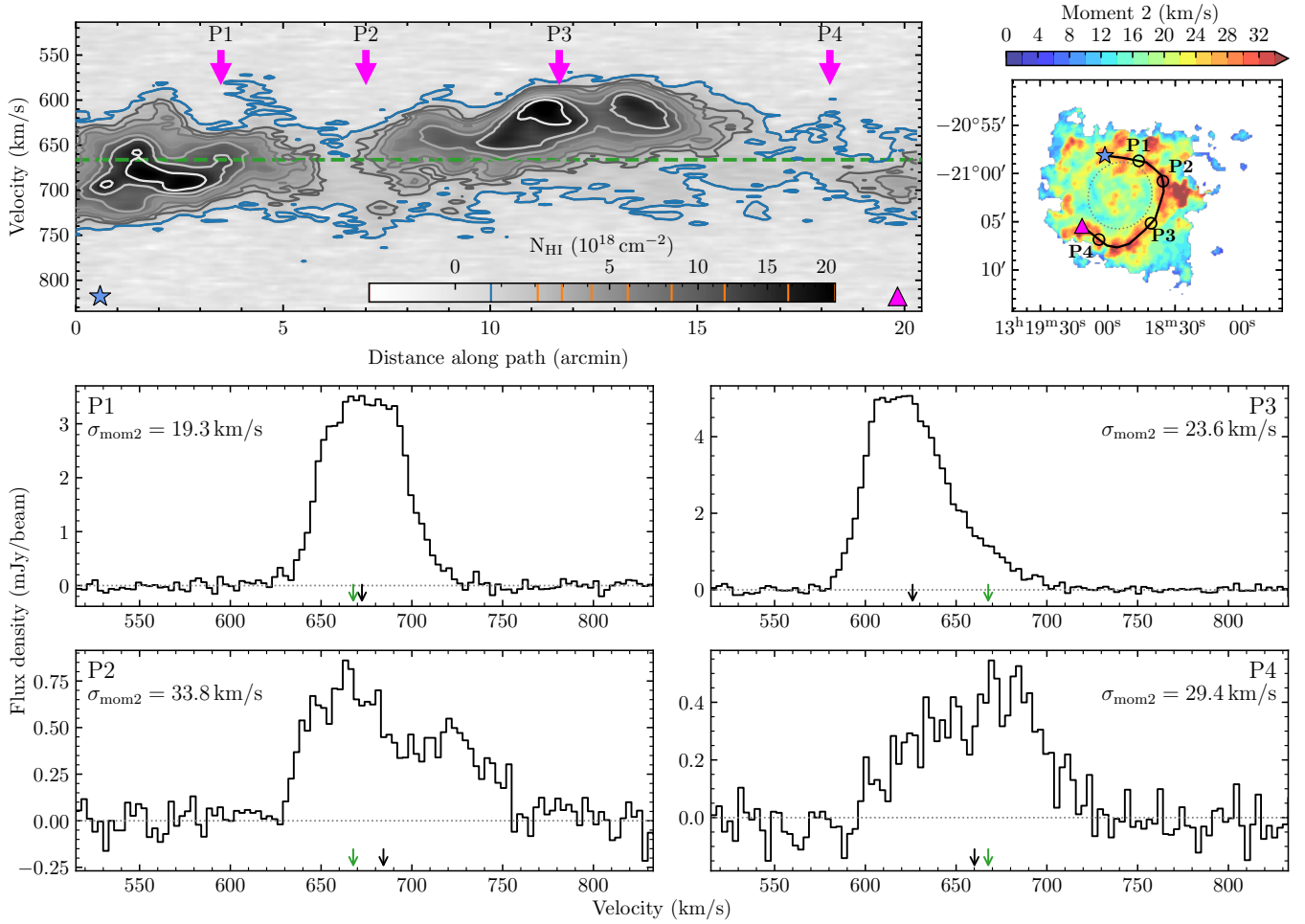
**Fig. 8.** Same as Fig. 7 but at an angle of  $224^\circ$  through the outer disk.



**Fig. 9.** Moment 2 map for NGC 5068 at  $21.6''$  resolution. Pixels with an HI column density below the  $S/N = 3$  threshold of  $N_{\text{HI}} = 5.9 \times 10^{18} \text{ cm}^{-2}$  are masked. The colourbar in the bottom of the image indicates the moment 2 velocity of the gas, the thin grey contours are spaced  $5 \text{ km s}^{-1}$  apart. The dotted magenta ellipse is centred on the optical centre of the galaxy and represents the optical size of the galaxy.

disk scenario is difficult to confirm. Throughout the rest of this work, we primarily refer to this component as the outer disk.

The northern region of the galaxy containing the clouds marked A, B, C in Figs. 2 and 6 makes up the third component. The kinematics of this region are not consistent with either the inner or outer disks, and thus we consider them a separate component.



**Fig. 10.** Top left: position-velocity (PV) diagram through the high moment 2 region of NGC 5068. The blue and orange lines in the greyscale colourbar correspond to the blue and greyscale contours. The green dashed line indicates the systemic velocity. Top right: moment 2 map of the galaxy with the black line tracing the path along which the PV slice was extracted, starting from the blue star and ending at the magenta triangle. Bottom: H I line profiles extracted at different locations along the PV slice, the extracted locations are indicated by the magenta arrows in the PV diagram. The location of each spectrum is also indicated by the labelled open circles on the moment 2 map. Green arrows at the bottom of the line profiles indicate the systemic velocity of the galaxy, while the black arrows point to the moment 1 velocity.

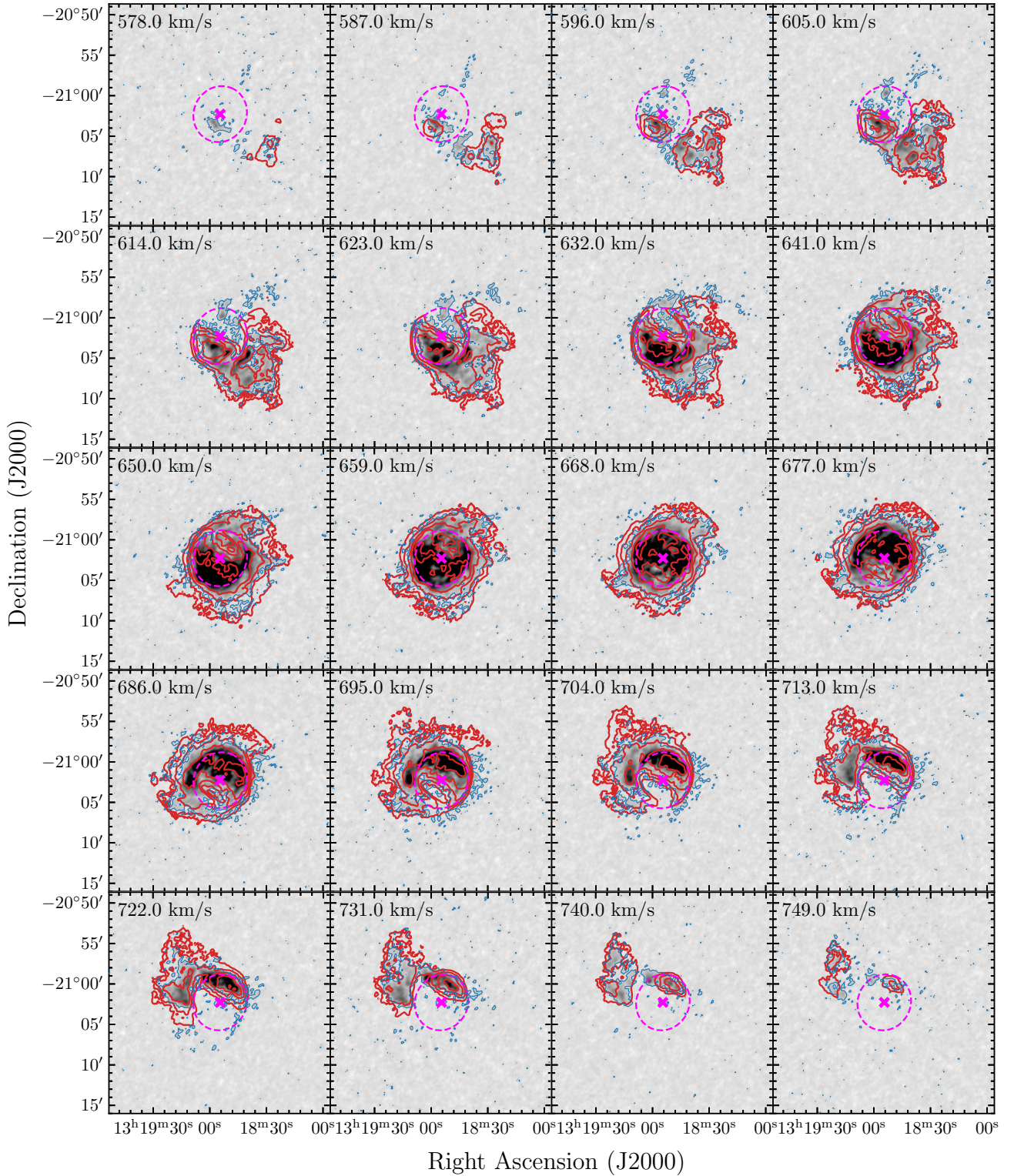
#### 4.1. High moment 2 ring

In Fig. 9, we present the second moment map at  $21.6''$  resolution for NGC 5068. The moment 2 can be used as a measure of the linewidth of the H I along each line of sight. In the case that the line profiles are Gaussian, then the moment 2 represents the velocity dispersion. Normally the velocity dispersion across the star forming disk is on average  $\sim 10$  to  $15 \text{ km s}^{-1}$  (e.g. Leroy et al. 2008). The median moment 2 value within the optical disk region (indicated by the dashed magenta ellipse in Fig. 9) is  $\sigma_v \sim 18 \text{ km s}^{-1}$ . Outside the optical disk, there are regions where the moment 2 values are significantly higher ( $\sigma_v > 25 \text{ km s}^{-1}$ ) than in the inner disk. There are a number of processes that can add energy to the interstellar medium of galaxies, and thus drive turbulence leading to an increase in the velocity dispersion. Many of these processes are associated with star formation activity, such as stellar feedback and supernova explosions (e.g. Tamburro et al. 2009; Krumholz & Burkhardt 2016). Since the high moment 2 values in NGC 5068 are found outside the stellar disk, it is likely that something other than star formation related processes is responsible for the high moment 2 values.

In order to investigate the source of the high moment 2 values, we take a PV slice 1 beam wide ( $21.6''$ ) through the ring of high moment 2 values on the outside edge of the optical disk region, where values range from  $\sigma_{\text{mom}2} \sim 22$  to  $35 \text{ km s}^{-1}$ . The PV diagram is presented in the top panel of Fig. 10. It is clear from this PV diagram, as well as the major axis PV diagram in Fig. 7, that there is low column density gas that spans a wide velocity range. It is probable that this broad low column density component is present throughout the H I disk of this system but is hidden in the moment 2 map due to much brighter narrow components, particularly in the inner disk region. However, this is not likely the cause of the high moment 2 ring on the edge of the optical disk.

In Fig. 10 we show four line profiles (P1 to P4) extracted at different points along the PV slice. These profiles show that there are multiple distinct overlapping components along the line of sight. This is particularly obvious in P2 and P4. Given that we already know that there are multiple components making up the overall H I disk for NGC 5068, it is likely that the multi-component profiles responsible for the high moment 2 ring are as a result of a superposition of the inner and outer disks. This could also explain the offset between the peaks of the different components in P2 and P4.





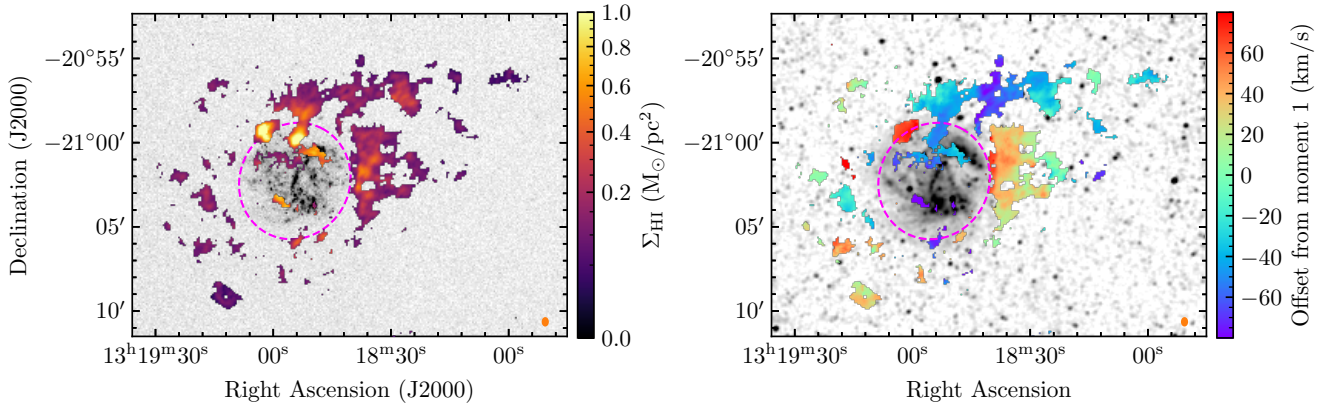
**Fig. 11.** Same as Fig. 4. The red contours ( $0.5\sigma_{\text{rms}}^{\text{data}} \times 2^n$ ,  $n = 0, 2, 4, \dots$ ) represent the inner and outer disk models generated with GALMOD.

#### 4.2. Modelling the $\text{H I}$ kinematics

In order to separate out the inner and outer disks from the third component so that we can investigate the origin of the  $\text{H I}$  in this system, it is necessary to create a model that describes the morphology and kinematics of the two disks. Modelling the velocity field of NGC 5068 using a tilted ring (Rogstad et al. 1974) model is not a trivial task, especially considering the degeneracy

of parameters such as position angle, inclination, and rotation velocity of almost face-on galaxies such as this one (Józsa et al. 2007).

As discussed in the previous section, there are at least three components to the total  $\text{H I}$  disk of this galaxy, however using a version of the GIPSY (Allen et al. 1985; van der Hulst et al. 1992) task GALMOD as implemented in 3DBAROLO (Di Teodoro & Fraternali 2015), we have built a



**Fig. 12.** Left: HI gas surface density of the clumpy gas not contained in the model overlaid on an GALEX FUV image of NGC 5068. Right: the velocity field of the clumpy gas overlaid on the MeerKAT continuum image, the colour shows difference in moment 1 velocity of the clumpy gas and the total velocity field shown in Fig. 6.

simple toy model describing the rotation of the inner and outer disks. For the inner disk, we used the inclination and position angle listed in Table 1 as measured from near-infrared imaging. The inclination of the outer disk was set to a constant of  $53^\circ$  which was estimated from the geometry of the outer HI contours.

We experimented with varying the velocity dispersion – using the average velocity dispersion in the different annuli, as well as different constant values (6 to  $20 \text{ km s}^{-1}$ ), but found it had no real impact on the final model. Thus the velocity dispersion was set to a constant  $15 \text{ km s}^{-1}$  for both the inner and outer disks as this is similar to the median value of the moment 2 map. The position angles for the warped outer disk, and the rotation velocities for both the inner and outer disk were derived from fits of the parameters to the data using the fitting task, 3DFIT, in 3DBAROLO. The centre for both the inner and outer disk was set to the optical centre which is consistent with the centre of the HI.

The resulting model is shown by the red contours overplotted on the channel maps in Fig. 11. The flux of the model is normalised by that of the data, and is therefore not an independent parameter. The threshold of the lowest red contour in Fig. 11 is chosen to match the  $3\sigma_{\text{rms}}$  (blue) contour of the data. We note that this simple model describes the two disks fairly well apart from the fingers noted in Fig. 4 and the clouds (A, B, C) to the N/NW of the galaxy which we did not include in the model.

In order to find the emission that is not well described by the model, we blank the data where the model is greater than  $0.5\sigma_{\text{rms}}$  or greater, this value corresponds to the lowest red contour in Fig. 11 which was chosen to match the  $3\sigma_{\text{rms}}$  data (blue) contour. This gives a “residual” data cube from which we can create the usual moment maps of the clumpy gas – the gas that is not described by either disk model. We impose two further restrictions on what we consider as part of the clumpy gas. The first requirement is to only include high signal-to-noise features in the residual maps, we do this by creating a S/N map using a linewidth of  $20 \text{ km s}^{-1}$ . All pixels in the moment 0 map with  $S/N < 5$  are excluded. The second requirement is that the values of the corresponding moment 2 map must be  $\text{mom2} < 40 \text{ km s}^{-1}$  – this is to exclude pixels where the emission could be due to wings of the line not being properly modelled. It would be interesting to see if any of the clumpy gas is related to star formation. We therefore compare the moment maps of the anomalous gas with GALEX FUV observations and radio continuum observations. Both are known to trace emission related

to recent or ongoing star formation. The FUV image is taken from the Survey for Ultraviolet emission in Neutral Gas Galaxies (SUNGG, Wong et al. 2016) which collated new and archival targeted observations for a sample of nearby galaxies. The HI surface density of the clumpy gas is shown overlaid on a GALEX FUV image of NGC 5068 in the left panel of Fig. 12, and the associated velocity field is overlaid on the MeerKAT continuum image in the right panel of Fig. 12.

From both panels of Fig. 12, we can see that spatially, the clumpy gas is mostly located outside of the main star forming disk, which suggests that this gas is likely not currently involved with any star formation activity. The total mass of this clumpy gas is  $M_{\text{clumpy}} = 2.6 \times 10^7 M_\odot$  (see Table 5). Since this gas was not included in the model, it is clearly not rotating with either the inner disk or the outer disk. The velocity field does show a velocity gradient in the different clumps, however it is unclear what the cause of the gradient may be. However it is evident that the clumpy gas on the northern side of the galaxy is responsible for driving the peculiar morphology of the velocity field in that region – see Fig. 6.

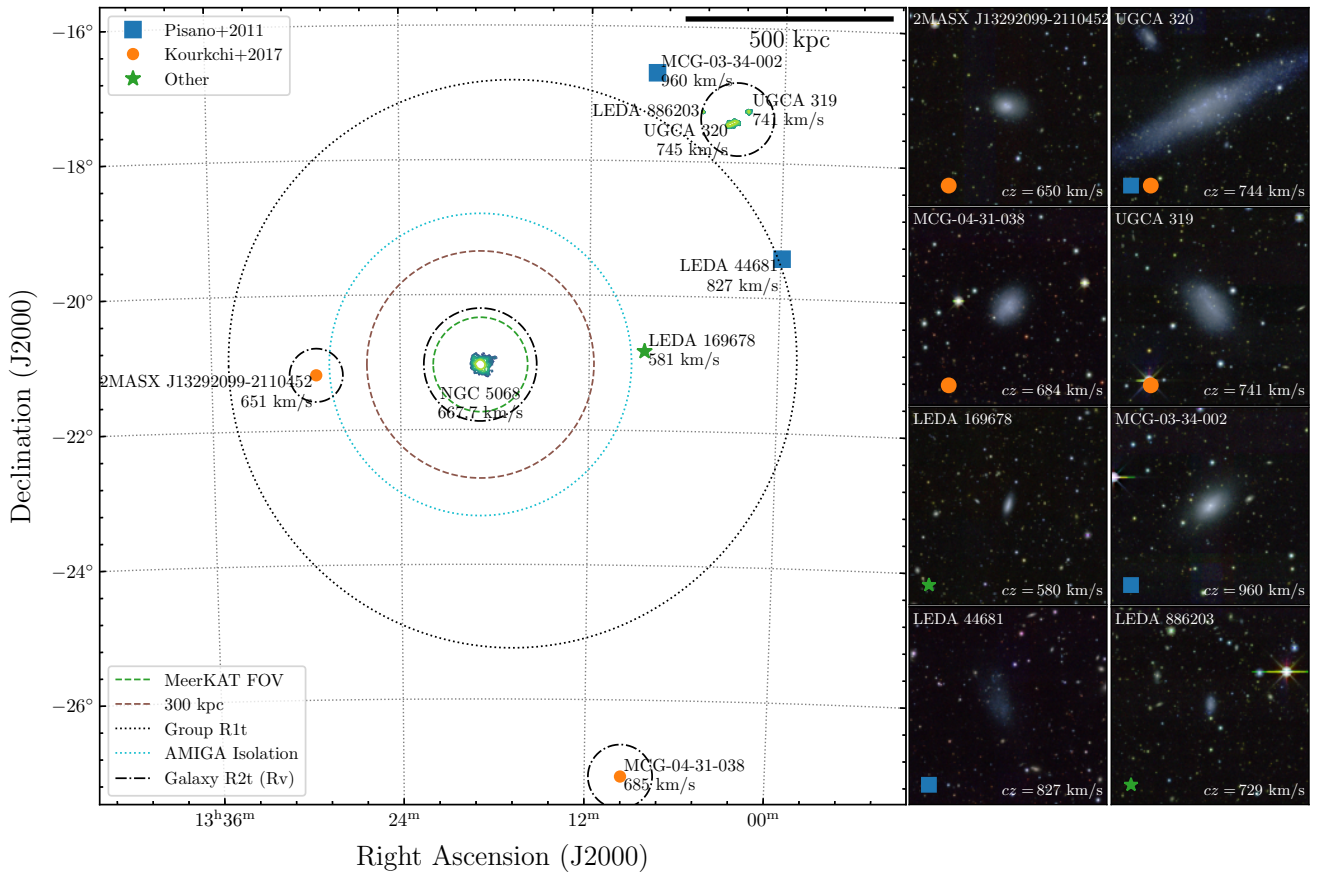
## 5. Origin of the anomalous gas

In the previous section, we have separated out the three components that comprise the HI of this system: 1 – the inner disk that is spatially coincident with the optical disk; 2 – the outer disk which has a kinematic warp, and due to its geometry relative to the inner disk could be considered a polar disk; 3 – the clumpy gas that is not described by either disk component. In this section we discuss a number of scenarios that could explain the origin of the peculiar behaviour of the HI in this system.

### 5.1. Interactions with nearby group galaxies

Figure 13 shows the eight spectroscopically confirmed galaxies within a  $5^\circ$  radius of NGC 5068. NGC 5068 was identified as part of a loose group of galaxies (Pisano et al. 2011), PGC 46400 (Kourkchi & Tully 2017). Karachentsev et al. (2017) measured the distances to NGC 5068 ( $5.2 \pm 0.2 \text{ Mpc}$ ), LEDA 44681 ( $7.2 \pm 0.3 \text{ Mpc}$ ), UGCA 320 ( $6.03 \text{ Mpc}$ ), and UGCA 319 ( $5.75 \text{ Mpc}$ ) using the redshift-independent tip of the red giant branch method. They conclude that UGCA 320 and UGCA 319 are an isolated pair that are dynamically separate from NGC 5068 and LEDA 44681.





**Fig. 13.** Nearby galaxies around NGC 5068. The galaxies marked with blue squares or orange circles were identified as group members with NGC 5068 by [Pisano et al. \(2011\)](#) and [Kourkchi & Tully \(2017\)](#). Left panel: sky distribution of the galaxies, the circles represent regions of different sizes used to determine isolation or identify group members. The R1t and R2t circles are taken from [Kourkchi & Tully \(2017\)](#) and are used to group sources together. The AMIGA ([Verdes-Montenegro et al. 2005](#)) isolation radius for NGC 5068 is represented by the dotted cyan circle. For reference, also plotted is the MeerKAT field of view (dashed green circle), and the brown dashed circle represents a radius of 300 kpc. The colour *giz* images on the right are  $5 \times 5$  arcmin<sup>2</sup> cutouts taken from DECaLS DR10.

The nearest two galaxies, 2MASX J13292099–2110452 and LEDA 169678, have a projected separation of 405 kpc and a velocity separation of  $17 \text{ km s}^{-1}$  and  $87 \text{ km s}^{-1}$  respectively. Despite these two close neighbours, NGC 5068 is classified as an isolated galaxy using the criteria of [Verdes-Montenegro et al. \(2005\)](#): there are no other galaxies with diameters between 1/4 and 4 times the diameter of the target that lie within a radius that is 20 times the diameter of the potential neighbour. This is based on the assumption that for a galaxy with a diameter of 25 kpc, an interloper of similar mass moving at a “field velocity” of  $150 \text{ km s}^{-1}$  would take 3 Gyr to close a separation of 20 times the interlopers diameter ( $\sim 500 \text{ kpc}$ )<sup>3</sup>.

The right panels of Fig. 13 show the composite *giz* images of the group galaxies (excluding NGC 5068) as observed by DECaLS DR10. The  $5 \times 5$  arcmin<sup>2</sup> colour images show a collection of blue galaxies that are significantly smaller on the sky than NGC 5068 which has a semi-major axis of  $7.03''$  (see Table 1). Over the redshift range of these galaxies,  $1''$  ranges from 40 pc to 57 pc. Based on the optical colours, sizes, and morphologies of this collection of galaxies, it is not likely even the closest two neighbours discussed above have ever interacted with NGC 5068.

<sup>3</sup> Gas orbital time of NGC 5068 is  $\sim 1$  Gyr, meaning that any gas would have settled following such an interaction.

## 5.2. Stripped gas from a passing neighbour

What if the anomalous gas is the result of a gas rich unidentified neighbour passing by NGC 5068 and losing all of its gas to NGC 5068? In such scenario the gas may have been stripped off the neighbour which continued on past NGC 5068, and part of the gas settled into the potential of NGC 5068 as the outer disk with the remainder of the gas remaining as clumps beyond the outer disk. We do not believe this to be a likely origin of the anomalous gas. Below we discuss why the scenario is improbable using simple assumptions based on the mass of the H I in the outer disk.

If the interaction had taken place, it would have been more than 1 Gyr in the past as the outer gas has already completed at least one orbit as it has settled into a disk-like component within the potential of NGC 5068. Given the H I mass of the outer gas ( $M_{\text{HI}} = 8.9 \times 10^7 M_{\odot}$ ), the stellar mass of the neighbour would be roughly  $4.45 \times 10^7 M_{\odot}$ , this assumes  $M_{\text{HI}}/M_{\star} = 2$ , which is consistent with the Small Magellanic Cloud ([Stanimirović et al. 1999](#)) and other dwarf galaxies ([Huang et al. 2012](#)). The stellar mass ratio between the two galaxies is 1:50, which means that the neighbour would not likely leave an imprint on NGC 5068 as a result of the interaction.

Using the  $M_{\text{HI}}-D_{\text{HI}}$  relation from [Wang et al. \(2016, Eq. \(2\)\)](#), and assuming the diameter of the optical disk is



$0.8 \times D_{\text{H I}}$ , we determine the neighbour is roughly  $D_{\text{opt}} \sim 4 \text{ kpc}$  ( $\sim 1.4'$  at 5.2 Mpc). With a conservative stellar mass to light ratio of 0.6, we calculate the mean  $r$ -band surface brightness of the neighbour to be  $\mu_r = 23.7 \text{ mag arcsec}^{-2}$ . If this neighbour passed by NGC 5068 with a maximum velocity of  $v = 100 \text{ km s}^{-1}$ , it would be located within a 100 kpc ( $36'$ ) radius after 1 Gyr. The  $5\sigma$  detection threshold in the DECaLS  $r$ -band image is  $\mu_r = 26.3 \text{ mag arcsec}^{-2}$  which means that the neighbour would be visible in the DECaLS data, however there is no likely candidate in the DECaLS imaging.

### 5.3. Minor merger with a gas rich galaxy

Since there is no neighbour in our search area, we consider if NGC 5068 underwent a merger with a gas-rich low mass satellite. Given the H I mass difference between the inner and outer disks, this would suggest a merging ratio of 1:10. Such an event would have to have taken place more than 1 Gyr ago as the outer H I has settled in the potential of NGC 5068. Minor mergers are usually defined as where the lower mass galaxy is more than four times less massive than the larger galaxy. Some studies (Lotz et al. 2008; Conselice 2006) have suggested that the timescales for minor mergers can vary from  $\tau \sim 0.3$  to 1 Gyr assuming an initial separation of 30 kpc. More recently, Conselice et al. (2022) have shown using hydrodynamical simulations that the timescale of mergers is also dependent on both redshift and mass ratio of the merging galaxies. Based on the Conselice et al. (2022) study, the merger timescale for a  $z \sim 0$  merger with a mass ratio of 1:10, could range between  $\tau \sim 1.7$  to 2 Gyr, however this assumes that the galaxies have  $M_\star > 10^9 M_\odot$ . Given that the H I in the NGC 5068 system has already settled, it is likely that if a minor merger had occurred it would have happened more than 2 Gyr ago. Despite the mass difference between the constituent galaxies, minor mergers are known to have an impact on the morphology and kinematics of the larger galaxy (e.g. Kazantzidis et al. 2009; Qu et al. 2011; Martin et al. 2018; Ghosh et al. 2022).

The optical morphology of NGC 5068 is undisturbed, and does not appear to have undergone any recent interactions. However it is possible that in such a scenario the main stellar disk of NGC 5068 was undisturbed. Mergers are thought to be one of the origin scenarios of polar disks (e.g. Stanonik et al. 2009, and references therein). While there is no clearly observable stellar component within the available deep optical imaging from DECaLS associated with the outer disk, it is possible that the outer disk could be caused by a minor merger and the associated stellar disk has been stretched out below detection limits. This scenario, however, does not explain the clouds which are a largely located on the northern side of the galaxy.

If all the anomalous gas (all H I gas not associated with the inner disk) from NGC 5068 could be traced back to one event such as a minor merger, given the time that has likely elapsed ( $>2$  Gyr), one would expect that the clouds would have settled into a more symmetric distribution around the galaxy. While we cannot conclusively rule out a minor merger as a possible origin scenario given that this scenario does not neatly explain all the gas, we do not assign this scenario a high probability of being the origin of the anomalous gas.

### 5.4. Fountain triggered accretion

Galactic fountains can be an important mechanism by which gas is recycled within a galaxy system (see, for example, Shapiro et al. 1976; Fraternali & Binney 2006): gas is expelled

from the main disk by processes associated with star formation such as supernovae and solar winds. The expelled gas mixes with the hotter gas in the halo and then the mixed gas cools and condenses before it is re-accreted onto the galaxy. This fountain driven accretion of gas means that the accreted gas contains both the original expelled gas, and gas from the halo, the net flow of the gas is into the galaxy. Given that this process arises as a result of activity in the stellar disk, the accreted gas is likely to be coincident with the stellar disk.

Simulations suggest that gas accreted onto the galaxy subsequent to mixing with gas ejected from the galaxy disk through fountain processes are likely to have a higher metal content than primordial gas (see review by Almeida et al. 2014; Brook et al. 2014; Tumlinson et al. 2017) which is thought to occur along filaments into the galaxy. Thus looking at the gas phase metallicity of the star forming regions on the edge of the galaxy disk, particularly where the anomalous gas and the star forming regions overlap, may provide some insight into the origin of gas (Howk et al. 2018).

NGC 5068 has been observed by a number of multi-wavelength surveys, but two surveys in particular have looked at the gas-phase metallicity of the star forming regions in NGC 5068: PHANGS-MUSE (Emsellem et al. 2022; Williams et al. 2022) and TYPHOON (Seibert et al., in prep.; Grasha et al. 2022). Both Williams et al. (2022) and Grasha et al. (2022) show that the metallicity of the gas in NGC 5068 cannot be explained by the simple radial model that describes the negative metallicity gradient seen in star-forming galaxies. Grasha et al. (2022, Fig. 3) in particular show that the H II regions on the northern side of the galaxy are more metal poor than regions at the same radius on the southern side of the galaxy.

Given the distribution of the star forming regions throughout NGC 5068 (see the background FUV and continuum images in Fig. 12), if fountain-driven accretion was responsible for the anomalous gas in NGC 5068, it is plausible that the distribution of the clumpy gas not explained by the disks would be more equally distributed around the galaxy. We conclude that while it is very likely that there are fountain-processes ongoing in NGC 5068, it is not the likely source of the anomalous H I gas.

### 5.5. Accretion of gas along a filament

The final scenario that we consider is that the anomalous gas is a result of gas accretion external to the galaxy halo. How this accretion occurs, and what the observational signatures of such accretion look like are still unclear. Simulations have shown that in galaxies the size of NGC 5068, accretion is expected to occur along filaments, condensing into clumps and clouds as it nears the galaxy disk (Kaufmann et al. 2006; van de Voort et al. 2011b; Wetzel & Nagai 2015; Cornuault et al. 2018; Iza et al. 2022).

Several observational signatures have been suggested as proof of these accretion modes. Due to the gas condensing as it reaches the H I disk, it is expected that the gas is accreted in clouds or clumps. Clouds or clumps with anomalous velocities have been observed around the Milky Way, these clouds, are known as intermediate (IVC) and high (HVC) velocity clouds (see review by Wakker & Van Woerden 1997; Wakker et al. 1999, and references therein). The clouds around the Milky Way have been shown to trace the flow of accreting gas, both as a result of extragalactic accretion (Wakker et al. 2007, 2008; Peek et al. 2008), and re-accretion of gas relating to a galactic fountain (McClure-Griffiths et al. 2013; Marasco et al. 2022).

The left panel of Fig. 12 shows that the anomalous gas associated with NGC 5068 is clumpy, it should be noted that

majority of this clumpy gas is very low column density ( $N_{\text{HI}} < 10^{19} \text{ cm}^{-2}$ ). As discussed in Sect. 3, the clouds on the north-western side of the galaxy range in HI mass from  $M_{\text{HI}} \sim 10^4 M_{\odot}$  to  $M_{\text{HI}} \sim 10^5 M_{\odot}$  which is consistent with the HI masses of the IVC/HVC complexes around the Galaxy (Wakker et al. 2008). The velocity field of the anomalous gas relative to the galaxy velocity field (see Fig. 6) is shown in the right panel of Fig. 12. The velocities of the anomalous gas show that the clouds coincident with the star-forming disk deviate from the overall rotation of the main HI disk.

In Sect. 5.3, we mentioned how mergers are one of the formation scenarios of polar disks. More recently, it has been shown that accretion could also trigger the formation of a polar disk, and this case an associated stellar component would not be expected (Macciò et al. 2006; Brook et al. 2008; Stanonik et al. 2009). Another feature present in polar disks when accretion is considered the origin, is kinematic warps (e.g. Brook et al. 2008). While the origin of the warps are not yet clear, it has been shown that they can be explained as the result of skewed angular momentum of gas accreting due to cosmic infall (Ostriker & Binney 1989; Jiang & Binney 1999; Sánchez-Salcedo 2006; Rand & Benjamin 2008).

Both the morphology and the kinematics of the anomalous gas in combination of the warped (possibly polar) outer disk of NGC 5068 point to ongoing accretion. It is interesting to note to that some of the clumpy gas is coincident with the optical disk right where there is some of the brightest star formation on the northern ridge of the galaxy. These star forming regions also have some of the lowest gas phase metallicity in the maps presented in Grasha et al. (2022).

Putting all of this together, we propose the following scenario: gas is being accreted along a filament that is aligned with the northern and north-western edge of the galaxy. This gas condenses into the clumps or clouds when it gets close to the galaxy disk, over time this accretion has given rise to what is now observable as the outer disk. Within this scenario, it is possible that not all the clouds feed the outer disk, but some are pulled into the star-forming disk enhancing the star formation on the northern side of galaxy.

## 6. Summary

In this paper we have presented new MeerKAT observations of the HI in NGC 5068 taken as part of the MeerKAT Large Survey Project, MHONGOOSE. The combination of the impressive sensitivity and resolution of these data have revealed a number of interesting features in the HI disk of NGC 5068. We have identified three separate components to the total HI disk: the inner disk, the outer disk which shows signatures of a kinematic warp and given the geometry could be a polar disk, and lastly the clumpy region to the north-western side of the galaxy. We constructed a model that contained a regularly rotating inner disk plus a more inclined warped outer disk that described the majority of the gas kinematics adequately. Using the model, we were able to isolate a significant amount of clumpy gas that was not well explained by the model of the disks. This clumpy gas accounts for  $\sim 2\%$  of the total HI mass of the system and also contains the clumps to the north and north-west of the galaxy.

We explored a number of different possible origin scenarios for the anomalous gas:

- Interaction with the nearby group galaxies – the projected distances between the galaxies make this an unlikely scenario.
- Stripped gas from a passing neighbour – assuming the neighbour survived the passage, we find no evidence for its existence.

- A minor merger with a gas rich neighbour – we cannot conclusively exclude this scenario, but do not believe it is the most likely scenario as it does not explain the presence of the clumpy gas on only one side of the galaxy.
- Fountain triggered accretion – accretion is likely, but this scenario would suggest a more metal enrichment than what is observed in the outer star forming regions, and for the clumpy gas distribution to follow the locations star forming regions.
- Accretion of gas along a filament – this scenario neatly explains the kinematics and morphology of all the anomalous HI.

While the last scenario is most likely based on the data we have presented in this paper, further detailed modelling of the gas is needed to understand if and how the gas is transported between the inner and outer disks. Unambiguous detection of cold mode accretion of gas onto galaxies will require the detection of HI gas at column densities of  $N_{\text{HI}} \sim 5 \times 10^{18} \text{ cm}^{-2}$  or lower, and at cloud scale resolution in combination of other tracers of cold gas such as Lyman- $\alpha$  (van de Voort & Schaye 2012; Ao et al. 2020; Kacprzak 2017). Simulations and some recent observations of high redshift galaxies suggest that Lyman- $\alpha$  emission traces cold gas being accreted onto the galaxies (e.g. Dijkstra & Loeb 2009; Daddi et al. 2021). However, with the currently available facilities, the ongoing MHONGOOSE survey provides the best chance of detecting and studying in detail, the low column density HI that could be linked to cold gas accretion.

**Acknowledgements.** We thank the anonymous referee for their constructive comments that improved the paper. We acknowledge useful discussions on the interpretation of this data with members of the MHONGOOSE team. J.H. thanks Nathan Deg for helpful discussions on polar ring galaxies. We thank the MeerLICHT team for their help with the MeerLICHT imaging, in particular: Paul Vreeswijk, Danielle Pieterse, Steven Bloemen, Paul Groot, and Patrick Woudt. Thanks to Filippo Fraternali and Thijs van der Hulst for useful discussions about the interpretation of the HI in this galaxy. This project has received funding from the European Research Council (ERC) under the European Union's Horizon 2020 research and innovation programme grant agreement no. 882793, project name MeerGas. P.K. acknowledges financial support by the German Federal Ministry of Education and Research (BMBF) Verbundforschung grant 05A20PC4 (Verbundprojekt D-MeerKAT-II). D.J.P. and N.Z. are supported through the South African Research Chairs Initiative of the Department of Science and Technology and National Research Foundation. K.S. acknowledges support from the Natural Sciences and Engineering Research Council of Canada (NSERC). B.K.G. acknowledges the financial support of the European Union's Horizon 2020 Research and Innovation Programme (ChETEC-INFRA – Project no. 101008324). L.V.M. acknowledges financial support from the grant CEX2021-001131-S funded by MCIN/AEI/10.13039/501100011033, from the grant PID2021-123930OB-C21 funded by MCIN/AEI/10.13039/501100011033, by “ERDF A way of making Europe” and by the European Union. L.C. acknowledges the financial support from the Chilean Agencia Nacional de Investigación y Desarrollo through the grant Fondecyt Regular 1210992. This paper makes use of MeerKAT data. The MeerKAT telescope is operated by the South African Radio Astronomy Observatory, which is a facility of the National Research Foundation, an agency of the Department of Science and Innovation. This research made use of Astropy (<http://www.astropy.org>), a community-developed core Python package for Astronomy (Astropy Collaboration 2013, 2018). Part of the data published here have been reduced using the CARACal pipeline, partially supported by ERC Starting grant number 679627 “FORNAX”, MAECI Grant Number ZA18GR02, DST-NRF Grant Number 113121 as part of the ISARP Joint Research Scheme, and BMBF project 05A17PC2 for D-MeerKAT. Information about CARACal can be obtained online under the URL: <https://caracal.readthedocs.io>

## References

- Allen, R. J., Ekers, R. D., & Terlou, J. P. 1985, in Data Analysis in Astronomy, Proceedings of the 1st Workshop held in Erice, eds. V. D. Gesù, L. Scarsi, P. Crane, J. Friedman, & S. Levialdi (New York: Plenum Press), *Ettore Majorana Int. Sci. Ser.*, 271

- Almeida, J. S., Elmegreen, B. G., Muñoz-Tuñón, C., & Elmegreen, D. M. 2014, *A&ARv*, **22**, 71
- Anand, G. S., Lee, J. C., Van Dyk, S. D., et al. 2021, *MNRAS*, **501**, 3621
- Ao, Y., Zheng, Z., Henkel, C., et al. 2020, *Nat. Astron.*, **4**, 670
- Arnaboldi, M., Oosterloo, T., Combes, F., Freeman, K. C., & Koribalski, B. 1997, *AJ*, **113**, 585
- Astropy Collaboration (Robitaille, T. P., et al.) 2013, *A&A*, **558**, A33
- Astropy Collaboration (Price-Whelan, A. M., et al.) 2018, *AJ*, **156**, 123
- Barnes, D. G., Staveley-Smith, L., De Blok, W. J. G., et al. 2001, *MNRAS*, **322**, 486
- Bigiel, F., Leroy, A., Walter, F., et al. 2008, *AJ*, **136**, 2846
- Bloemen, S., Groot, P., Woudt, P., et al. 2016, *SPIE Conf. Ser.*, **9906**, 990664
- Boomsma, R., Oosterloo, T. A., Fraternali, F., Van Der Hulst, J. M., & Sancisi, R. 2008, *A&A*, **490**, 555
- Bosma, A. 2016, *Formation and Evolution of Galaxy Outskirts* (Cambridge: Cambridge University Press)
- Brook, C. B., Governato, F., Quinn, T., et al. 2008, *ApJ*, **689**, 678
- Brook, C. B., Stinson, G., Gibson, B. K., et al. 2014, *MNRAS*, **443**, 3809
- Cadiou, C., Dubois, Y., & Pichon, C. 2022, *MNRAS*, **514**, 5429
- Conselice, C. J. 2006, *ApJ*, **638**, 686
- Conselice, C. J., Mundy, C. J., Ferreira, L., & Duncan, K. 2022, *ApJ*, **940**, 168
- Cornuault, N., Lehnert, M. D., Boulanger, F., & Guillard, P. 2018, *A&A*, **610**, A75
- Daddi, E., Valentino, F., Rich, R. M., et al. 2021, *A&A*, **649**, A78
- de Blok, W. J., Keating, K. M., Pisano, D. J., et al. 2014, *A&A*, **569**, A68
- de Blok, W. J., Adams, E. A., Amram, P., et al. 2016, *Proceedings of MeerKAT Science: On the Pathway to the SKA*, 7
- de Blok, W. J., Athanassoula, E., Bosma, A., et al. 2020, *A&A*, **643**, A147
- de Blok, W. J. G., Healy, J., Maccagni, F. M., et al. 2024, *A&A*, in press, <https://doi.org/10.1051/0004-6361/202348297>
- Deul, E. R., & den Hartog, R. H. 1990, *A&A*, **229**, 362
- Dey, A., Schlegel, D. J., Lang, D., et al. 2019, *AJ*, **157**, 168
- Di Teodoro, E. M., & Fraternali, F. 2014, *A&A*, **567**, A68
- Di Teodoro, E. M., & Fraternali, F. 2015, *MNRAS*, **451**, 3021
- Dijkstra, M., & Loeb, A. 2009, *MNRAS*, **400**, 1109
- Emsellem, E., Schinnerer, E., Santoro, F., et al. 2022, *A&A*, **659**, A191
- English, J. 2017, *Int. J. Mod. Phys. D*, **26**, 2017
- Fraternali, F., & Binney, J. J. 2006, *MNRAS*, **366**, 449
- Fraternali, F., Oosterloo, T., Sancisi, R., & van Moorsel, G. 2001, *ApJ*, **562**, L47
- Fraternali, F., van Moorsel, G., Sancisi, R., & Oosterloo, T. 2002, *AJ*, **123**, 3124
- Gentile, G., Józsa, G. I., Serra, P., et al. 2013, *A&A*, **554**, A125
- Ghosh, S., Saha, K., Jog, C. J., Combes, F., & Di Matteo, P. 2022, *MNRAS*, **511**, 5878
- Gottesman, S. T., & Mahon, M. E. 1990, *Int. Astron. Union Colloq.*, **124**, 209
- Grasha, K., Chen, Q. H., Battisti, A. J., et al. 2022, *ApJ*, **929**, 118
- Grobler, T. L., Nunhokee, C. D., Smirnov, O. M., van Zyl, A. J., & de Bruyn, A. G. 2014, *MNRAS*, **439**, 4030
- Hafen, Z., Faucher-Giguère, C. A., Anglés-Alcázar, D., et al. 2020, *MNRAS*, **494**, 3581
- Heald, G., & Team, H. 2014, *Proc. Int. Astron. Union*, **10**, 69
- Heald, G., Józsa, G., Serra, P., et al. 2011, *A&A*, **526**, A118
- Hess, K. M., Pisano, D. J., Wilcots, E. M., & Chengalur, J. N. 2009, *ApJ*, **699**, 76
- Ho, S. H., Martin, C. L., & Turner, M. L. 2019, *ApJ*, **875**, 54
- Howk, J. C., Rueff, K. M., Lehner, N., et al. 2018, *ApJ*, **856**, 166
- Huang, S., Haynes, M. P., Giovanelli, R., & Brinchmann, J. 2012, *ApJ*, **756**, 113
- Huang, S., Katz, N., Davé, R., et al. 2019, *MNRAS*, **484**, 2021
- Iza, F. G., Scannapieco, C., Nuza, S. E., et al. 2022, *MNRAS*, **517**, 832
- Jiang, I. G., & Binney, J. 1999, *MNRAS*, **303**, L7
- Jonas, J. L., & MeerKAT Team 2016, *Proc. Sci.*, **277**, 1
- Józsa, G. I. G., Kenn, F., Klein, U., & Oosterloo, T. A. 2007, *A&A*, **468**, 731
- Józsa, G. I. G., White, S. V., Thorat, K., et al. 2020, *ASP Conf. Ser.*, **527**, 635
- Kacprzak, G. G. 2017, *Astrophys. Space Sci. Lib.*, **430**, 145
- Kamphuis, J., & Sancisi, R. 1993, *A&A*, **273**, L31
- Kamphuis, P., Jütte, E., Heald, G. H., et al. 2022, *A&A*, **668**, A182
- Karachentsev, I. D., Makarova, L. N., Tully, R. B., et al. 2017, *MNRAS*, **469**, L113
- Kaufmann, T., Mayer, L., Wadsley, J., Stadel, J., & Moore, B. 2006, *MNRAS*, **370**, 1612
- Kazantzidis, S., Zentner, A. R., Kravtsov, A. V., Bullock, J. S., & Debattista, V. P. 2009, *ApJ*, **700**, 1896
- Kereš, D., Katz, N., Weinberg, D. H., & Davé, R. 2005, *MNRAS*, **363**, 2
- Kereš, D., Katz, N., Fardal, M., Davé, R., & Weinberg, D. H. 2009, *MNRAS*, **395**, 160
- Koribalski, B. S., Staveley-Smith, L., Kilborn, V. A., et al. 2004, *AJ*, **128**, 16
- Kourkchi, E., & Tully, R. B. 2017, *ApJ*, **843**, 16
- Krumholz, M. R., & Burkhardt, B. 2016, *MNRAS*, **458**, 1671
- Lang, P., Meidt, S. E., Rosolowsky, E., et al. 2020, *ApJ*, **897**, 122
- Larson, R. B. 1972, *Nature*, **236**, 21
- Lauberts, A., & Valentijn, E. A. 1989, *The Messenger*, **56**, 31
- Leroy, A. K., Walter, F., Brinks, E., et al. 2008, *AJ*, **136**, 2782
- Leroy, A. K., Sandstrom, K. M., Lang, D., et al. 2019, *ApJS*, **244**, 24
- Li, A., Fraternali, F., Marasco, A., et al. 2023, *MNRAS*, **520**, 147
- Lotz, J. M., Jonsson, P., Cox, T. J., & Primack, J. R. 2008, *MNRAS*, **391**, 1137
- Macciò, A. V., Moore, B., & Stadel, J. 2006, *ApJ*, **636**, L25
- Marasco, A., Fraternali, F., Heald, G., et al. 2019, *A&A*, **631**, A50
- Marasco, A., Fraternali, F., Lehner, N., & Howk, J. C. 2022, *MNRAS*, **515**, 4176
- Martin, G., Kaviraj, S., Devriendt, J. E., Dubois, Y., & Pichon, C. 2018, *MNRAS*, **480**, 2266
- McClure-Griffiths, N. M., Green, J. A., Hill, A. S., et al. 2013, *ApJ*, **770**, L4
- Melioli, C., Brighenti, F., D'Ercole, A., & De Gouveia Dal Pino, E. M. 2008, *MNRAS*, **388**, 573
- Melioli, C., Brighenti, F., D'Ercole, A., & De Gouveia Dal Pino, E. M. 2009, *MNRAS*, **399**, 1089
- Meurer, G. R., Hanish, D. J., Ferguson, H. C., et al. 2006, *ApJS*, **165**, 307
- Meyer, M. J., Zwaan, M. A., Webster, R. L., et al. 2004, *MNRAS*, **350**, 1195
- Meyer, M., Robotham, A., Obreschkow, D., et al. 2017, *PASA*, **34**, e052
- Nelson, D., Vogelsberger, M., Genel, S., et al. 2013, *MNRAS*, **429**, 3353
- Nelson, D., Genel, S., Vogelsberger, M., et al. 2015, *MNRAS*, **448**, 59
- Offringa, A. R., & Smirnov, O. 2017, *MNRAS*, **471**, 301
- Offringa, A. R., McKinley, B., Hurley-Walker, N., et al. 2014, *MNRAS*, **444**, 606
- Oosterloo, T., Fraternali, F., & Sancisi, R. 2007, *AJ*, **134**, 1019
- Ostriker, E. C., & Binney, J. J. 1989, *MNRAS*, **237**, 785
- Peek, J. E. G., Putman, M. E., & Sommer-Larsen, J. 2008, *ApJ*, **674**, 227
- Pisano, D. J., Barnes, D. G., Staveley-Smith, L., et al. 2011, *ApJS*, **197**, 28
- Qu, Y., Di Matteo, P., Lehnert, M. D., Van Driel, W., & Jog, C. J. 2011, *A&A*, **535**, A5
- Ramesh, R., Nelson, D., & Pillepich, A. 2023, *MNRAS*, **518**, 5754
- Rand, R. J., & Benjamin, R. A. 2008, *ApJ*, **676**, 991
- Rogstad, D. H., Lockart, I. A., & Wright, M. C. H. 1974, *ApJ*, **193**, 309
- Rosolowsky, E., Hughes, A., Leroy, A. K., et al. 2021, *MNRAS*, **502**, 1218
- Sánchez-Salcedo, F. J. 2006, *MNRAS*, **365**, 555
- Sancisi, R., Fraternali, F., Oosterloo, T., & Van Der Hulst, T. 2008, *A&ARv*, **15**, 189
- Sardone, A., Pisano, D. J., Pingel, N. M., et al. 2021, *ApJ*, **910**, 69
- Schmidt, T. M., Bigiel, F., Klessen, R. S., & de Blok, W. J. 2016, *MNRAS*, **457**, 2642
- Serra, P., Westmeier, T., Giese, N., et al. 2015, *MNRAS*, **448**, 1922
- Shapiro, P. R., Field, G. B., Shapiro, P. R., & Field, G. B. 1976, *ApJ*, **205**, 762
- Sorgho, A., Carignan, C., Pisano, D. J., et al. 2019, *MNRAS*, **482**, 1248
- Stanimirović, S., Staveley-Smith, L., Dickey, J. M., Sault, R. J., & Snowden, S. L. 1999, *MNRAS*, **302**, 417
- Stanonić, K., Platen, E., Aragón-Calvo, M. A., et al. 2009, *ApJ*, **696**, L6
- Swaters, R. A., Sancisi, R., & van der Hulst, J. M. 1997, *ApJ*, **491**, 140
- Tamburro, D., Rix, H. W., Leroy, A. K., et al. 2009, *AJ*, **137**, 4424
- Tumlinson, J., Peebles, M. S., & Werk, J. K. 2017, *ARA&A*, **55**, 389
- van der Byl, A., Smith, J., Martens, A., et al. 2022, *J. Astron. Telesc. Instrum. Syst.*, **8**, 011006
- van der Hulst, J. M., Terlou, J. P., Begeman, K. G., et al. 1992, in *Astronomical Data Analysis Software and Systems*, eds. D. M. Worrall, C. Biemesderfer, & J. Barnes, *ASP Conf. Ser.*, **25**, 131
- van de Voort, F., & Schaye, J. 2012, *MNRAS*, **423**, 2991
- van de Voort, F., Schaye, J., Booth, C. M., & Dalla Vecchia, C. 2011a, *MNRAS*, **415**, 2782
- van de Voort, F., Schaye, J., Booth, C. M., Haas, M. R., & Dalla Vecchia, C. 2011b, *MNRAS*, **414**, 2458
- van de Voort, F., Springel, V., Mandelker, N., van den Bosch, F. C., & Pakmor, R. 2019, *MNRAS*, **482**, L85
- van Driel, W., Combes, F., Casoli, F., et al. 1995, *AJ*, **109**, 942
- Vargas, C. J., Heald, G., Walterbos, R. A. M., et al. 2017, *ApJ*, **839**, 118
- Verdes-Montenegro, L., Sulentic, J., Lisenfeld, U., et al. 2005, *A&A*, **436**, 443
- Veronese, S., de Blok, W. J. G., & Walter, F. 2023, *A&A*, **672**, A55
- Wakker, B. P., & Van Woerden, H. 1997, *ARA&A*, **35**, 217
- Wakker, B. P., van Woerden, H., & Gibson, B. K. 1999, *ASP Conf. Ser.*, **166**, 311
- Wakker, B. P., York, D. G., Howk, J. C., et al. 2007, *ApJ*, **670**, L113
- Wakker, B. P., York, D. G., Wilhelm, R., et al. 2008, *ApJ*, **672**, 298
- Walter, F., Brinks, E., Blok, W. J. G. D., et al. 2008, *AJ*, **136**, 2563
- Wang, J., Koribalski, B. S., Serra, P., et al. 2016, *MNRAS*, **460**, 2143
- Westmeier, T., Kiteff, S., Pallot, D., et al. 2021, *MNRAS*, **506**, 3962
- Wetzel, A. R., & Nagai, D. 2015, *ApJ*, **808**, 40
- Wijnholds, S. J., Grobler, T. L., & Smirnov, O. M. 2016, *MNRAS*, **457**, 2331
- Williams, T. G., Kreckel, K., Belfiore, F., et al. 2022, *MNRAS*, **509**, 1303
- Wong, O. I., Meurer, G. R., Zheng, Z., et al. 2016, *MNRAS*, **460**, 1106